

Contents lists available at ScienceDirect

Journal of Computational Physics

www.elsevier.com/locate/jcp



A novel fully-decoupled, second-order time-accurate, unconditionally energy stable scheme for a flow-coupled volume-conserved phase-field elastic bending energy model



Xiaofeng Yang ¹

Department of Mathematics, University of South Carolina, Columbia, SC 29208, USA

ARTICLE INFO

Article history: Received 11 July 2020 Received in revised form 16 November 2020 Accepted 17 November 2020 Available online 2 February 2021

Keywords:
Phase-field
Fully-decoupled
Second-order
Allen-Cahn
Nonlocal
Unconditional energy stability

ABSTRACT

Different from the classical phase-field elastic bending model of lipid vesicles that uses a penalty term to conserve volume approximately, in this paper, a new model with accurate volume conservation is first established. Then, for its coupling system with the incompressible flow, we design a highly efficient scheme which is linear and energy stable. More importantly, this scheme is second-order time-accurate and fully-decoupled and it only needs to solve several independent linear equations with constant coefficients at each time step to obtain a numerical solution with second-order time accuracy. The key idea is to introduce two types of nonlocal auxiliary variables, one of which is linearize the nonlinear potential, and the other is used to introduce an ordinary differential equation to deal with the nonlinear coupling terms that satisfy the "zero-energy-contribution" feature. We strictly prove the solvability and unconditional energy stability and conduct numerical simulations in 2D and 3D to demonstrate the accuracy and stability of the scheme numerically. To the best of the author's knowledge, the decoupling method developed in this paper is the first second-order fully-decoupled scheme for the flow-coupled phase-field model.

© 2020 Published by Elsevier Inc.

1. Introduction

In cell biology, vesicles refer to a class of relatively small intracellular cystic structures. The periphery of vesicles is composed of at least one lipid bilayer molecular membrane, which is used to store, digest, or transport substances (such as cell products or waste). Starting from the classic work of Du et al. in [8–10], the phase-field (diffusive interface) method has been used to simulate the structural deformation of lipid vesicles under various situations, see [1,12,22,33,35,39]. The main idea of the phase-field approach is to use a scalar variable to represent the two fluid components separated by a vesicle membrane, and use the bending energy formulation to replace the average curvature of the membrane surface. By minimizing the total free energy in some specific space (usually using the L^2 space, called Allen-Cahn relaxation dynamics or mean curvature flow), the so-called phase-field elastic bending energy model is derived (PFEBE model, for short). Besides, if the fluid characteristics of the vesicle and its surrounding fluid (such as the flow behavior driven by shear or gravity) need to be considered, the Navier-Stokes equation and the PFEBE model are coupled through the elastic stress and advection terms to form a full flow-coupled model.

E-mail address: xfyang@math.sc.edu.

¹ X. Yang' work was partially supported by NSF-DMS-1720212 and DMS-1818783 and DMS-2012490.

It is worth noting that in order to ensure the conservation of volume and surface area over time, in the classic PFEBE model proposed by Du et al. [8-10], two penalty energy potentials are added into the total free energy of the system, so the total volume and surface area can be approximately preserved. Therefore, in practice, if a good conservation effect of the surface area and volume is desired, a large penalty parameter needs to be adopted. However, such a penalty method has some disadvantages which are described as follows by taking the volume conservation as an example since it is much simpler to conserve the volume than the surface area. First, no matter how large the penalty parameter is, the volume can only remain roughly the same. Second, using a larger penalty parameter will increase the stiffness of the system, resulting in severe time-step constraints and higher computational costs. Some efforts have been made in this direction to conserve the volume precisely. The Lagrange multiplier method is developed in [1,36], but because the model does not follow the energy structure, it is very challenging to develop efficient numerical schemes. Another effort was made in [17], which uses the well-known volume conservation system Cahn-Hilliard dynamics to reconstruct the model. However, it brings up a disadvantage that the generated system has two more orders than the Allen-Cahn system, so it is relatively difficult to solve. Therefore, in this paper, the first goal is to use Allen-Cahn dynamics to reconstruct the PFEBE model so that the volume can be conserved accurately over time. To this end, we eliminate the penalty potential for volume in the free energy and add a nonlocal term directly to the original PDE system. This term not only eliminates the volume change but also helps to retrieve almost the same energy dissipation format as the original system.

Next, we consider the numerical approximation of the new vesicle model coupled with the hydrodynamics. We remember so far that for the classical PFEBE model, many successful attempts have been made in algorithm design or numerical simulation, such as the Invariant Energy Quadratization (IEQ) method [38], Scalar Auxiliary Variable (SAV) method [5], linear stabilization method [6], nonlinear functional derivative method [17], Exponential Time Differencing (ETD) method [36], etc. However, compared with the partial model containing only one phase-field equation, the full flow-coupled vesicle model has received less attention due to its highly nonlinear coupling nature. As we all know, as the main component of the full flow-coupled vesicle model, the Navier-Stokes equation has many effective numerical methods, such as the projection/Gauge/penalty methods (cf. [13–16,24,25,29]). Thus, one might think that as long as the above-mentioned known methods for the PFEBE model are combined with the methods for the Navier-Stokes equations, an effective numerical method for the full flow coupling model can be obtained.

However, unfortunately, the current situation is that, not only for the full flow-coupled vesicle model discussed in this paper, but also for almost all hydrodynamically coupled phase-field models, to the best of the author's knowledge, there are currently no numerical schemes with the second-order time-accuracy, fully-decoupling, and energy stability. There is a lack of sufficient skills to achieve such a scheme, and the main difficulty lies in how to discretize the advection and stress terms that are common in almost all hydrodynamically coupled phase-field models. For these two terms, the popular discretization method is to use fully-implicit or semi-implicit methods, but they inevitably lead to expensive fully-coupled schemes, see [3,7,11,18,19,31]. As far as the author knows, the only fully-decoupled scheme was developed in [23] and some follow-up works in [17,30–32]. Its main idea is to add a stabilization term to the explicit advection velocity so that the momentum equation and phase-field equation can be decoupled. However, the disadvantage of this method is that the added stabilization term contains implicitly processed chemical potential, which leads to the need to solve the phase-field equation with variable coefficients at each time step, resulting in higher calculation costs than that with constant coefficients. Meanwhile, the scheme developed in [17,23,30–32] is only first-order time-accurate, and it seems quite challenging to extend the stabilization idea to the second-order version.

Therefore, the second purpose of this paper is to develop a new numerical scheme for the full flow-coupled volumeconserved phase-field model for lipid vesicles, so that it is not only unconditionally energy stable, linear, and secondorder time accurate, but also fully-decoupled. We expect that the designed scheme only needs to solve several linearly independent equations with constant coefficients at each time step, thereby reducing the actual calculation cost. To this end, based on the existing effective methods (including the projection method to solve the coupling of pressure and velocity, and the SAV method that linearizes the nonlinear energy potential), we make full use of an obvious but often overlooked property, the so-called "zero-energy-contribution" feature satisfied by the advection and stress to construct a new type of fully-decoupled scheme. Thus, from a new perspective, we introduce a novel idea of introducing a nonlocal variable and designing an ordinary differential equation related to it, which contains the inner products of the advection/stress and some specific functions. This ODE is trivial at the continuous level because all the terms contained therein are zero terms. But after discretization, it can help eliminate all the troublesome nonlinear terms that are explicitly handled, thereby obtaining unconditional energy stability. Besides, the introduction of the nonlocal variable can decompose each discrete equation into multiple sub-equations that can be solved independently. Therefore, a fully-decoupled structure is obtained. We also give a rigorous proof of unconditional energy stability and further simulate various numerical examples in 2D and 3D to demonstrate stability and accuracy numerically. To the best of the author's knowledge, the decoupling method developed in this paper is not only the first second-order fully-decoupled scheme for the particular flow-coupled vesicle model but also applicable to any coupling type models with "zero-energy-contribution" terms.

We organize the rest of the article in the following way. In Section 2, we develop the new flow-coupled volume-conserved vesicle model and then present its energy law. In Section 3, we propose a fully-decoupled, second-order time-marching numerical method and give a detailed implementation method. We prove the solvability and unconditional energy stability as well. In Section 4, numerous numerical experiments in 2D and 3D are conducted to demonstrate the effectiveness of the model and the proposed numerical scheme. Section 5 gives some concluding remarks.

2. The full flow-coupled volume-conserved PFEBE model

Based on the total free energy given in Du et al.'s classic PFEBE model [8–10], we develop a new flow-coupled model that can guarantee the volume conservation over time. First, we define the phase-field variable as $\phi(\mathbf{x}) = \tanh\left(\frac{d(\mathbf{x})}{\sqrt{2\epsilon}}\right)$ for all $\mathbf{x} \in \Omega$, where $d(\mathbf{x})$ is the signed distance between a point \mathbf{x} and the membrane surface Γ , and ϵ is the width of the diffusive interface. In such a framework, the postulated total free energy for the hydrodynamically-coupled PFEBE model is given as follows [9]:

$$E(\mathbf{u},\phi) = \int_{\Omega} \frac{1}{2} |\mathbf{u}|^2 d\mathbf{x} + \lambda \left(\int_{\Omega} \frac{\epsilon}{2} (\Delta \phi - f(\phi))^2 d\mathbf{x} + \frac{1}{2} M (A(\phi) - \beta)^2 \right), \tag{2.1}$$

where **u** is the average velocity field ($\mathbf{u} = (u_1, u_2)$ for 2D, and $\mathbf{u} = (u_1, u_2, u_3)$ for 3D), λ is a normalization constant that characterizes the magnitude of bending energy, $F(\phi) = \frac{1}{4\epsilon^2}(\phi^2 - 1)^2$ is the double-well potential, $f(\phi) = F'(\phi) = \frac{1}{\epsilon^2}\phi(\phi^2 - 1)$, and $A(\phi)$ is the surface area function that is defined as

$$A(\phi) = \epsilon \int_{\Omega} \left(\frac{1}{2} |\nabla \phi|^2 + F(\phi) \right) d\mathbf{x}. \tag{2.2}$$

The surface area can be given as $\frac{3}{2\sqrt{2}}A(\phi)$. $M\gg 1$ is a positive penalty parameter. β denotes a constant related to the initial surface area, and we set $\beta=A(\phi^0)$ with $\phi^0=\phi(t=0)$ in the paper.

By using the L^2 gradient flow approach (i.e., the Allen-Cahn relaxation dynamics), we obtain the following dynamical system:

$$\phi_t + (\mathbf{u} \cdot \nabla)\phi + \gamma \left(\mu - \frac{1}{|\Omega|} \int_{\Omega} \mu d\mathbf{x}\right) = 0, \tag{2.3}$$

$$\mu = \epsilon(\Delta - f'(\phi))(\Delta\phi - f(\phi)) + \epsilon M(A(\phi) - \beta)(-\Delta\phi + f(\phi)), \tag{2.4}$$

$$\mathbf{u}_t + (\mathbf{u} \cdot \nabla)\mathbf{u} + \nabla p - \nu \Delta \mathbf{u} - \lambda \mu \nabla \phi = 0, \tag{2.5}$$

$$\nabla \cdot \mathbf{u} = 0, \tag{2.6}$$

where $f'(\phi) = \frac{1}{\epsilon^2}(3\phi^2 - 1)$, γ is the relaxation mobility parameter, $\mu = \frac{1}{\lambda}\frac{\delta E}{\delta \phi}$ is the scaled variational derivative or chemical potential, $\mu \nabla \phi$ is the induced stress using the generalized Fick's law, and $(\mathbf{u} \cdot \nabla)\phi$ is the fluid advection.

Remark 2.1. Note that the volume of the vesicle is defined as $\int_{\Omega} \frac{1+\phi}{2} d\mathbf{x}$, see [1,8–10], hence, by computing the L^2 -inner product of (2.3) with 1, and using the integration by parts and the divergence-free condition (2.6), we derive

$$\frac{d}{dt} \int \phi d\mathbf{x} = 0, \tag{2.7}$$

which means the model (2.3) retains the exact volume. It can be seen that the nonlocal term $-\frac{1}{|\Omega|}\int_{\Omega}\mu d\mathbf{x}$ added in (2.3) plays a key role in maintaining the total volume of ϕ . This idea was originally ingeniously proposed in [27], with the aim of developing the conservative Allen-Cahn equation.

We consider one of the following two types of boundary conditions:

(i) all variables are periodic, or (ii)
$$\mathbf{u}|_{\partial\Omega} = \mathbf{0}$$
, $\partial_{\mathbf{n}}\phi|_{\partial\Omega} = \partial_{\mathbf{n}}\Delta\phi|_{\partial\Omega} = 0$, (2.8)

where **n** is the unit outward normal on the boundary $\partial \Omega$. The initial conditions read as

$$\mathbf{u}|_{(t=0)} = \mathbf{u}^0, \ p|_{(t=0)} = p^0, \phi|_{(t=0)} = \phi^0. \tag{2.9}$$

The system (2.3)-(2.6) admits the law of energy dissipation, which can be obtained by the following process. We multiply the inner product of (2.3) by $\lambda\mu$ in L^2 to derive

$$\lambda(\phi_t, \mu) = -\lambda \gamma \left\| \mu - \frac{1}{|\Omega|} \int_{\Omega} \mu d\mathbf{x} \right\|^2 - \lambda \int_{\Omega} (\mathbf{u} \cdot \nabla) \phi \mu d\mathbf{x}, \tag{2.10}$$

where we use

$$\begin{split} &(\mu - \frac{1}{|\Omega|} \int\limits_{\Omega} \mu d\mathbf{x}, \mu) \\ &= (\mu - \frac{1}{|\Omega|} \int\limits_{\Omega} \mu d\mathbf{x}, \mu - \frac{1}{|\Omega|} \int\limits_{\Omega} \mu d\mathbf{x}) + (\mu - \frac{1}{|\Omega|} \int\limits_{\Omega} \mu d\mathbf{x}, \frac{1}{|\Omega|} \int\limits_{\Omega} \mu d\mathbf{x}) \\ &= \left\| \mu - \frac{1}{|\Omega|} \int\limits_{\Omega} \mu d\mathbf{x} \right\|^2, \end{split}$$

since $(\mu - \frac{1}{|\Omega|} \int_{\Omega} \mu d\mathbf{x}, 1) = 0$. Taking the inner product of (2.4) with $-\lambda \phi_t$ in L^2 , we get

$$-\lambda(\mu,\phi_t) + \frac{d}{dt}\lambda\left(\int\limits_{\Omega} \frac{\epsilon}{2}(\Delta\phi - f(\phi))^2 d\mathbf{x} + \frac{1}{2}M(A(\phi) - \beta)^2 d\mathbf{x}\right) = 0.$$
 (2.11)

Taking the inner product of (2.5) with $\bf u$ in L^2 , and using integration by parts and (2.6), we obtain

$$\frac{d}{dt} \int_{\Omega} \frac{1}{2} |\mathbf{u}|^2 d\mathbf{x} + \nu \|\nabla \mathbf{u}\|^2 = \lambda \int_{\Omega} \mu \nabla \phi \cdot \mathbf{u} d\mathbf{x} - \int_{\Omega} (\mathbf{u} \cdot \nabla) \mathbf{u} \cdot \mathbf{u} d\mathbf{x}. \tag{2.12}$$

Combining the above three equations (2.10)-(2.12), we obtain the energy dissipation law as

$$\frac{d}{dt}E(\mathbf{u},\phi) = -\lambda\gamma \left\| \mu - \frac{1}{|\Omega|} \int_{\Omega} \mu d\mathbf{x} \right\|^2 - \nu \|\nabla \mathbf{u}\|^2, \tag{2.13}$$

where the two negative terms on the right end specify the diffusion rate of the total free energy $E(\mathbf{u}, \phi)$.

Remark 2.2. We note that when deriving (2.13), the nonlinear integrals related to advection, advection, and stress are all canceled out. More precisely, the following two identities hold

$$\int_{\Omega} (\mu \nabla \phi \cdot \mathbf{u} - (\mathbf{u} \cdot \nabla) \phi \mu) d\mathbf{x} = 0, \quad \int_{\Omega} (\mathbf{u} \cdot \nabla) \mathbf{u} \cdot \mathbf{u} d\mathbf{x} = 0,$$
(2.14)

where the second one is due to the divergence-free condition (2.6) and integration by parts. The two identities mean that these nonlinear terms do not contribute to the total free energy or energy diffusivity, that is, they satisfy the "zero-energy-contribution" property. We will take advantage of it when developing the decoupling type scheme in the next section.

Remark 2.3. For the sake of completeness, here we provide the classical PFEBE model with the volume potential, which was developed in [8–10]. The model uses two penalization potentials to enforce the surface area and volume conservation approximately. Therefore, the postulated free energy reads as

$$\widetilde{E}(\mathbf{u},\phi) = E(\mathbf{u},\phi) + \frac{1}{2}\widetilde{M}(V(\phi) - V(\phi^0))^2,$$
(2.15)

where $V(\phi) = \int_{\Omega} \frac{\phi + 1}{2} d\mathbf{x}$, and $\widetilde{M} \gg 1$ is the penalty parameter. Note that no matter how big \widetilde{M} is, the volume can only be conserved approximately.

3. Numerical scheme

We are now developing a numerical scheme to solve the volume-conserved flow-coupled PFEBE model (2.3)-(2.6). The main challenge is how to construct the decoupling method. Moreover, considering the efficiency and accuracy of the algorithm in practice, we also expect the scheme to satisfy linearity, second-order time accuracy, and unconditional energy stability. The detailed process for developing this scheme is given as follows.

3.1. Reformulation to an equivalent system

First, we introduce a nonlocal variable Q(t) and design a special time-evolving ODE that reads as

$$\begin{cases}
Q_t = \int\limits_{\Omega} \left(\lambda(\mathbf{u} \cdot \nabla) \phi \mu - \lambda \mu \nabla \phi \cdot \mathbf{u} + (\mathbf{u} \cdot \nabla) \mathbf{u} \cdot \mathbf{u} \right) d\mathbf{x}, \\
Q|_{(t=0)} = 1,
\end{cases}$$
(3.1)

with $\nabla \cdot \mathbf{u} = 0$ and \mathbf{u} satisfy the boundary conditions (2.8). Using (2.14), the ODE is equivalent to the trivial ODE that reads as

$$\begin{cases}
Q_t = 0, \\
Q|_{(t=0)} = 1.
\end{cases}$$
(3.2)

It is obvious that $Q_1(t) = 1$ is the solution.

Second, we introduce another nonlocal variable U(t) such that:

$$U(t) = \sqrt{\int_{\Omega} \frac{1}{2} (\Delta \phi - f(\phi))^2 d\mathbf{x} + \frac{1}{2\epsilon} M(A(\phi) - \beta)^2 + B},$$
(3.3)

where B > 0. This is the so-called SAV method [4,5,28,40,41] which is an efficient method to linearize the nonlinear terms induced by the energy potentials.

Then, we rewrite the PDE system (2.3)-(2.6) using the variables (\mathbf{u} , p, μ , ϕ , U, Q) as:

$$\phi_t + Q(\mathbf{u} \cdot \nabla)\phi + \gamma \left(\mu - \frac{1}{|\Omega|} \int_{\Omega} \mu d\mathbf{x}\right) = 0, \tag{3.4}$$

$$\mu = \epsilon H U, \tag{3.5}$$

$$\mathbf{u}_t + Q(\mathbf{u} \cdot \nabla)\mathbf{u} + \nabla p - \nu \Delta \mathbf{u} - \lambda Q \mu \nabla \phi = 0, \tag{3.6}$$

$$\nabla \cdot \mathbf{u} = 0, \tag{3.7}$$

$$U_t = \frac{1}{2} \int_{\Omega} H \phi_t d\mathbf{x},\tag{3.8}$$

$$Q_t = \int_{\Omega} \left(\lambda(\mathbf{u} \cdot \nabla) \phi \mu - \lambda \mu \nabla \phi \cdot \mathbf{u} + (\mathbf{u} \cdot \nabla) \mathbf{u} \cdot \mathbf{u} \right) d\mathbf{x}, \tag{3.9}$$

where the function $H(\phi)$ is defined as:

$$H(\phi) = \frac{(\Delta - f'(\phi))(\Delta\phi - f(\phi)) + M(A(\phi) - \beta)(-\Delta\phi + f(\phi))}{\sqrt{\int_{\Omega} \frac{1}{2} (\Delta\phi - f(\phi))^2 d\mathbf{x} + \frac{1}{2\epsilon} M(A(\phi) - \beta)^2 + B}}.$$
(3.10)

Remark 3.1. We make some modifications to the original system (2.3)-(2.6) to obtain the new system (3.4)-(3.9). First, we rewrite (2.4) with the new variables U, and take the time derivative of U to obtain (3.8). Second, we add three inner products containing advection and stress with some specific functions into the ODE (3.2) to obtain (3.9). The two ODEs, (3.9) and (3.2), are equivalent because the integral terms in (3.9) are simply equal to zero from (2.14). Third, for the advection and stress terms satisfying the "zero-energy-contribution" feature, we multiply them with the nonlocal variable Q in (3.4) and (3.6) since $Q \equiv 1$. Therefore, the new system using the variables (\mathbf{u} , p, μ , ϕ , U, Q) is equivalent to the original system (2.3)-(2.6) using the variables (\mathbf{u} , p, μ , ϕ).

The boundary conditions of the new system (3.4)-(3.9) are still (2.8). Note that the equations (3.8) and (3.9) for the new variables U and Q are only time-dependent, so no boundary conditions are needed. The initial conditions of the system (3.4)-(3.9) are set as follows,

$$\begin{cases} \mathbf{u}|_{(t=0)} = \mathbf{u}^{0}, \, p|_{(t=0)} = p^{0}, \, \phi|_{(t=0)} = \phi^{0}, \\ U|_{(t=0)} = \sqrt{\int\limits_{\Omega} \frac{1}{2} (\Delta \phi^{0} - f(\phi^{0}))^{2} d\mathbf{x} + \frac{1}{2\epsilon} M(A(\phi^{0}) - \beta)^{2} + B}, \, Q|_{(t=0)} = 1. \end{cases}$$
(3.11)

The new system (3.4)-(3.9) also holds the energy dissipation law that can be obtained through a similar process obtaining (2.13). Since the discrete energy stability proof process follows the same principle, we show the following detailed process to make it clear. We multiply the L^2 inner product of (3.4) with $\lambda\mu$ to get

$$\lambda(\phi_t, \mu) = -\lambda \gamma \left\| \mu - \frac{1}{|\Omega|} \int_{\Omega} \mu d\mathbf{x} \right\|^2 - \lambda Q \int_{\Omega} (\mathbf{u} \cdot \nabla) \phi \mu d\mathbf{x}. \tag{3.12}$$

Taking the inner product of (3.5) with $-\lambda \phi_t$ in L^2 , we get

$$-\lambda(\mu,\phi_t) = -\epsilon \lambda U \int_{\Omega} H\phi_t d\mathbf{x}. \tag{3.13}$$

Taking the inner product of (3.6) with \mathbf{u} in L^2 , and using integration by parts and (3.7), we obtain

$$\frac{d}{dt} \int_{\Omega} \frac{1}{2} |\mathbf{u}|^2 d\mathbf{x} + \nu \|\nabla \mathbf{u}\|^2 = \lambda Q \int_{\Omega} \mu \nabla \phi \cdot \mathbf{u} d\mathbf{x} - Q \int_{\Omega} (\mathbf{u} \cdot \nabla) \mathbf{u} \cdot \mathbf{u} d\mathbf{x}. \tag{3.14}$$

Multiplying (3.8) with $2\lambda \in U$, we get

$$\lambda \epsilon \frac{d}{dt} (|U|^2) = \epsilon \lambda U \int_{\Omega} H \phi_t d\mathbf{x}. \tag{3.15}$$

Multiplying (3.9) with Q, we get

$$\frac{d}{dt}(\frac{1}{2}|Q|^2) = \lambda Q \int_{\Omega} (\mathbf{u} \cdot \nabla)\phi \mu d\mathbf{x} - \lambda Q \int_{\Omega} \mu \nabla \phi \cdot \mathbf{u} d\mathbf{x} + Q \int_{\Omega} (\mathbf{u} \cdot \nabla)\mathbf{u} \cdot \mathbf{u} d\mathbf{x}.$$
(3.16)

Combining (3.12)-(3.16) and noting that all two terms marked with the same Greek letters are canceled, we derive the energy law as follows:

$$\frac{d}{dt}E(\mathbf{u},\phi,U,Q) = -\lambda\gamma \left\| \mu - \frac{1}{|\Omega|} \int_{\Omega} \mu d\mathbf{x} \right\|^2 - \nu \|\nabla \mathbf{u}\|^2, \tag{3.17}$$

where

$$E(\mathbf{u}, \phi, U, Q) = \int_{\Omega} \frac{1}{2} |\mathbf{u}|^2 d\mathbf{x} + \lambda \epsilon |U|^2 + \frac{1}{2} |Q|^2.$$
(3.18)

Remark 3.2. In the process of deriving the energy law for the new model (3.4)-(3.9), we no longer need the two integral terms formed by the advection and stress to cancel each other as (2.14), because the newly added ODE (3.9) contains corresponding terms that can cancel them separately. In other words, when developing a stable discrete scheme, we can discretize the advection and stress using different methods, which makes it possible to design a fully-decoupled scheme.

3.2. Numerical scheme

We are now ready to develop a second-order semi-discrete scheme to solve the system (3.4)-(3.9). Given (\mathbf{u} , p, μ , ϕ , U, Q)ⁿ⁻¹ and (\mathbf{u} , p, μ , ϕ , U, Q)ⁿ⁺¹ as follows.

Step 1: we compute $(\tilde{\mathbf{u}}, \mu, \phi, U, O)^{n+1}$ by

$$\frac{a\phi^{n+1} - b\phi^n + c\phi^{n-1}}{2\delta t} + Q^{n+1}(\mathbf{u}^* \cdot \nabla)\phi^* + \gamma \left(\mu^{n+1} - \frac{1}{|\Omega|} \int_{\Omega} \mu^{n+1} d\mathbf{x}\right) = 0,$$
(3.19)

$$\mu^{n+1} = \epsilon H^* U^{n+1} + \frac{S_1}{\epsilon^3} (\phi^{n+1} - \phi^*)$$

$$- \frac{S_2}{\epsilon} \Delta (\phi^{n+1} - \phi^*) + \epsilon S_3 \Delta^2 (\phi^{n+1} - \phi^*),$$
(3.20)

$$\frac{a\tilde{\mathbf{u}}^{n+1} - b\mathbf{u}^n + c\mathbf{u}^{n-1}}{2\delta t} + Q^{n+1}(\mathbf{u}^* \cdot \nabla)\mathbf{u}^* - \nu \Delta \tilde{\mathbf{u}}^{n+1} + \nabla p^n - \lambda Q^{n+1}\mu^* \nabla \phi^* = 0, \tag{3.21}$$

$$aU^{n+1} - bU^n + cU^{n-1} = \frac{1}{2} \int_{\Omega} H^*(a\phi^{n+1} - b\phi^n + c\phi^{n-1}) d\mathbf{x}, \tag{3.22}$$

$$\frac{aQ^{n+1} - bQ^n + cQ^{n-1}}{2\delta t} = \int_{\Omega} \left(\lambda(\mathbf{u}^* \cdot \nabla)\phi^* \mu^{n+1} - \lambda \mu^* \nabla \phi^* \cdot \tilde{\mathbf{u}}^{n+1} + (\mathbf{u}^* \cdot \nabla)\mathbf{u}^* \cdot \tilde{\mathbf{u}}^{n+1} \right) d\mathbf{x}. \tag{3.23}$$

Step 2: we compute p^{n+1} , \mathbf{u}^{n+1} by

$$\frac{a}{28t}(\mathbf{u}^{n+1} - \tilde{\mathbf{u}}^{n+1}) + \nabla(p^{n+1} - p^n) = 0, \tag{3.24}$$

$$\nabla \cdot \mathbf{u}^{n+1} = 0. \tag{3.25}$$

In the above scheme.

$$a = 3, b = 4, c = 1, \mathbf{u}^* = 2\mathbf{u}^n - \mathbf{u}^{n-1}, \phi^* = 2\phi^n - \phi^{n-1},$$

 $H^* = H(\phi^*), \mu^* = 2\mu^n - \mu^{n-1},$

 S_1 , S_2 , S_3 are positive stabilization parameters, and the boundary conditions are either periodic or the physical boundary conditions as

$$\partial_{\mathbf{n}}\phi^{n+1}|_{\partial\Omega} = \partial_{\mathbf{n}}\Delta\phi^{n+1}|_{\partial\Omega} = 0, \ \tilde{\mathbf{u}}^{n+1}|_{\partial\Omega} = \mathbf{0}, \ \mathbf{u}^{n+1} \cdot \mathbf{n}|_{\partial\Omega} = 0. \tag{3.26}$$

We explain some details of the scheme (3.19)-(3.25) in the following remarks.

Remark 3.3. The scheme is linear, and it uses implicit and explicit combination method to deal with all nonlinear terms. For the hydrodynamical equations, we use the second-order pressure correction scheme (3.21)-(3.24)-(3.25) (cf. [34]), of which $\tilde{\mathbf{u}}^{n+1}$ is the intermediate velocity following the Dirichlet boundary conditions (or periodic) and the final velocity field \mathbf{u}^{n+1} follows the divergence-free condition. To obtain the pressure, we just apply the divergence operator to (3.24) and then obtain the following Poisson equation for p^{n+1} , i.e.,

$$-\Delta p^{n+1} = -\frac{a}{2\delta t} \nabla \cdot \tilde{\mathbf{u}}^{n+1} - \Delta p^n, \tag{3.27}$$

with the periodic boundary condition or $\partial_{\mathbf{n}} p^{n+1}|_{\partial\Omega} = 0$. Once p^{n+1} is computed from (3.27), we update \mathbf{u}^{n+1} by using (3.24), i.e.,

$$\mathbf{u}^{n+1} = \tilde{\mathbf{u}}^{n+1} - \frac{2\delta t}{a} \nabla (p^{n+1} - p^n). \tag{3.28}$$

Note that the homogeneous Neumann boundary condition is assumed for the pressure p^{n+1} . Some recent work in [2, 20]can preserve the second-order accuracy by employing Neumann boundary conditions for the velocity with the projection method.

Remark 3.4. The initialization of the second-order scheme requires all values at $t=t^1$, which can be obtained by constructing the first-order scheme based on the backward Euler method. In the above second-order scheme (3.19)-(3.25), as long as we set $a=2, b=2, c=0, \psi^*=\psi^n$ for any variable ψ , the first-order scheme can be easily obtained. Moreover, by using mathematical induction, it is easy to conclude that the following volume conservation property holds:

$$\int_{\Omega} \phi^{n+1} d\mathbf{x} = \int_{\Omega} \phi^n d\mathbf{x} = \dots = \int_{\Omega} \phi^0 d\mathbf{x}.$$
 (3.29)

Remark 3.5. Three extra second-order linear stabilizers (associated with S_1 , S_2 , and S_3) are added in the scheme. Note that the coefficient $H(\phi)$ contains almost all explicitly processed terms, including the fourth-order term $\Delta^2 \phi$. As we all know, the explicit processing method used for high-order linear terms is unstable, so we have to restore the higher-order terms by using the second-order stabilizer with the comparable magnitude, which is why the S_3 term is added. The use of S_1 and S_2 is due to the similar reasons and these two terms are used to balance the explicit processed terms $f^2(\phi)$ and $\Delta f(\phi)$ contained in $H(\phi)$, respectively. In Section 4, we provide numerical evidence to show that these stabilizers are critical for enhancing the stability of the numerical scheme while using large time steps, see Fig. 4.8 (e).

3.3. Implementation process and solvability

Now, we discuss how to implement the scheme (3.19)-(3.25). Since (3.24)-(3.25) in step 2 is the standard step of the projection method, we only need to consider the implementation of step 1. The scheme (3.19)-(3.23) in step 1 does not look like the fully-decoupled scheme we expect, because in each step, the unknowns are still coupled together. Furthermore, the scheme also contains a large number of nonlocal operations, which may bring difficulties to the actual calculation. Therefore, in practice, we need to decouple all variables and get rid of all nonlocal computations, which can be achieved by the following steps.

First, we use the nonlocal variable Q^{n+1} to split $(\phi, \mu, U)^{n+1}$ into a linear combination form that reads as

$$\begin{cases} \phi^{n+1} = \phi_1^{n+1} + Q^{n+1}\phi_2^{n+1}, \\ \mu^{n+1} = \mu_1^{n+1} + Q^{n+1}\mu_2^{n+1}, \\ U^{n+1} = U_1^{n+1} + Q^{n+1}U_2^{n+1}. \end{cases}$$
(3.30)

Then the scheme (3.19)-(3.20) can be rewritten as

$$\begin{cases} \frac{a(\phi_{1}^{n+1}+Q^{n+1}\phi_{2}^{n+1})}{2\delta t} + Q^{n+1}(\mathbf{u}^{*}\cdot\nabla)\phi^{*} \\ + \gamma\left(\mu_{1}^{n+1}+Q^{n+1}\mu_{2}^{n+1} - \frac{1}{|\Omega|}\int_{\Omega}(\mu_{1}^{n+1}+Q^{n+1}\mu_{2}^{n+1})d\mathbf{x}\right) = \frac{b\phi^{n}-c\phi^{n-1}}{2\delta t}, \\ \mu_{1}^{n+1}+Q^{n+1}\mu_{2}^{n+1} = \epsilon H^{*}(U_{1}^{n+1}+Q^{n+1}U_{2}^{n+1}) \\ + \frac{S_{1}}{\epsilon^{3}}(\phi_{1}^{n+1}+Q^{n+1}\phi_{2}^{n+1}-\phi^{*}) - \frac{S_{2}}{\epsilon}\Delta(\phi_{1}^{n+1}+Q^{n+1}\phi_{2}^{n+1}-\phi^{*}) \\ + \epsilon S_{3}\Delta^{2}(\phi_{1}^{n+1}+Q^{n+1}\phi_{2}^{n+1}-\phi^{*}). \end{cases}$$
(3.31)

ding to Q^{n+1} , the system (3.31) can be split into two sub-systems as

According to Q^{n+1} , the system (3.31) can be split into two sub-systems as

$$\begin{cases} \frac{a}{2\delta t}\phi_{1}^{n+1} + \gamma \left(\mu_{1}^{n+1} - \frac{1}{|\Omega|} \int_{\Omega} \mu_{1}^{n+1} d\mathbf{x}\right) = \frac{b\phi^{n} - c\phi^{n-1}}{2\delta t}, \\ \mu_{1}^{n+1} = \epsilon H^{*}U_{1}^{n+1} + \frac{S_{1}}{\epsilon^{3}}(\phi_{1}^{n+1} - \phi^{*}) - \frac{S_{2}}{\epsilon} \Delta(\phi_{1}^{n+1} - \phi^{*}) + \epsilon S_{3}\Delta^{2}(\phi_{1}^{n+1} - \phi^{*}), \end{cases}$$
(3.32)

and

$$\begin{cases}
\frac{a}{2\delta t}\phi_{2}^{n+1} + \gamma \left(\mu_{2}^{n+1} - \frac{1}{|\Omega|} \int_{\Omega} \mu_{2}^{n+1} d\mathbf{x}\right) = -(\mathbf{u}^{*} \cdot \nabla)\phi^{*}, \\
\mu_{2}^{n+1} = \epsilon H^{*} U_{2}^{n+1} + \frac{S_{1}}{\epsilon^{3}} \phi_{2}^{n+1} - \frac{S_{2}}{\epsilon} \Delta \phi_{2}^{n+1} + \epsilon S_{3} \Delta^{2} \phi_{2}^{n+1}.
\end{cases} (3.33)$$

By taking the L^2 inner product of the first equation in (3.32) and (3.33) with 1, using (3.29), and noting $\nabla \cdot \mathbf{u}^* = 0$, we immediately get

$$\int_{\Omega} \phi_1^{n+1} d\mathbf{x} = \int_{\Omega} \phi^n d\mathbf{x} = \int_{\Omega} \phi^{n-1} d\mathbf{x} = \int_{\Omega} \phi^* d\mathbf{x}, \qquad \int_{\Omega} \phi_2^{n+1} d\mathbf{x} = 0.$$
(3.34)

The boundary conditions of the ϕ_1^{n+1} and ϕ_2^{n+1} are either periodic or

$$\partial_{\mathbf{n}}\phi_{1}^{n+1}|_{\partial\Omega} = \partial_{\mathbf{n}}\Delta\phi_{1}^{n+1}|_{\partial\Omega} = 0, \ \partial_{\mathbf{n}}\phi_{2}^{n+1}|_{\partial\Omega} = \partial_{\mathbf{n}}\Delta\phi_{2}^{n+1}|_{\partial\Omega} = 0. \tag{3.35}$$

Second, using the nonlocal variables U_1^{n+1} and U_2^{n+1} , we split the variables $(\phi_1, \phi_2, \mu_1, \mu_2)^{n+1}$ as the following form

$$\begin{cases} \phi_1^{n+1} = \phi_{11}^{n+1} + U_1^{n+1} \phi_{12}^{n+1}, & \mu_1^{n+1} = \mu_{11}^{n+1} + U_1^{n+1} \mu_{12}^{n+1}, \\ \phi_2^{n+1} = \phi_{21}^{n+1} + U_2^{n+1} \phi_{22}^{n+1}, & \mu_2^{n+1} = \mu_{21}^{n+1} + U_2^{n+1} \mu_{22}^{n+1}. \end{cases}$$
(3.36)

Replacing $(\phi_1, \phi_2, \mu_1, \mu_2)^{n+1}$ in (3.32) and (3.33) using (3.36), and according to U_1^{n+1} and U_2^{n+1} , we obtain the following four subsystems,

$$\begin{cases}
\frac{a}{2\delta t}\phi_{11}^{n+1} + \gamma \left(\mu_{11}^{n+1} - \frac{1}{|\Omega|} \int_{\Omega} \mu_{11}^{n+1} d\mathbf{x}\right) = \frac{b\phi^{n} - c\phi^{n-1}}{2\delta t}, \\
\mu_{11}^{n+1} = \frac{S_{1}}{\epsilon^{3}}\phi_{11}^{n+1} - \frac{S_{2}}{\epsilon} \Delta\phi_{11}^{n+1} + \epsilon S_{3}\Delta^{2}\phi_{11}^{n+1} - \left(\frac{S_{1}}{\epsilon^{3}}\phi^{*} - \frac{S_{2}}{\epsilon}\Delta\phi^{*} + \epsilon S_{3}\Delta^{2}\phi^{*}\right),
\end{cases} (3.37)$$

$$\begin{cases} \frac{a}{2\delta t}\phi_{12}^{n+1} + \gamma \left(\mu_{12}^{n+1} - \frac{1}{|\Omega|} \int_{\Omega} \mu_{12}^{n+1} d\mathbf{x}\right) = 0, \\ \mu_{12}^{n+1} = \frac{S_1}{\epsilon^3}\phi_{12}^{n+1} - \frac{S_2}{\epsilon} \Delta \phi_{12}^{n+1} + \epsilon S_3 \Delta^2 \phi_{12}^{n+1} + \epsilon H^*, \end{cases}$$
(3.38)

$$\begin{cases}
\frac{a}{2\delta t}\phi_{21}^{n+1} + \gamma \left(\mu_{21}^{n+1} - \frac{1}{|\Omega|} \int_{\Omega} \mu_{21}^{n+1} d\mathbf{x}\right) = -(\mathbf{u}^* \cdot \nabla)\phi^*, \\
\mu_{21}^{n+1} = \frac{S_1}{\epsilon^3}\phi_{21}^{n+1} - \frac{S_2}{\epsilon} \Delta\phi_{21}^{n+1} + \epsilon S_3 \Delta^2\phi_{21}^{n+1},
\end{cases}$$
(3.39)

and

$$\begin{cases} \frac{a}{2\delta t}\phi_{22}^{n+1} + \gamma \left(\mu_{22}^{n+1} - \frac{1}{|\Omega|} \int_{\Omega} \mu_{22}^{n+1} d\mathbf{x}\right) = 0, \\ \mu_{22}^{n+1} = \frac{S_1}{\epsilon^3}\phi_{22}^{n+1} - \frac{S_2}{\epsilon} \Delta \phi_{22}^{n+1} + \epsilon S_3 \Delta^2 \phi_{22}^{n+1} + \epsilon H^*. \end{cases}$$
(3.40)

The boundary conditions of the above four system read as

$$\partial_{\mathbf{n}}(\phi_{11}, \phi_{12}, \phi_{21}, \phi_{22})^{n+1}|_{\partial\Omega} = 0, \, \partial_{\mathbf{n}}\Delta(\phi_{11}, \phi_{12}, \phi_{21}, \phi_{22})^{n+1}|_{\partial\Omega} = 0.$$
(3.41)

By taking the L^2 inner product of the first equation in the above four subsystems with 1, using (3.29), and noting $\nabla \cdot \mathbf{u}^* = 0$, we immediately get

$$\int_{\Omega} \phi_{11}^{n+1} d\mathbf{x} = \int_{\Omega} \phi^{n} d\mathbf{x} = \int_{\Omega} \phi^{n-1} d\mathbf{x} = \int_{\Omega} \phi^{*} d\mathbf{x},$$

$$\int_{\Omega} \phi_{12}^{n+1} d\mathbf{x} = \int_{\Omega} \phi_{21}^{n+1} d\mathbf{x} = \int_{\Omega} \phi_{22}^{n+1} d\mathbf{x} = 0.$$
(3.42)

To solve the above four systems (3.37)-(3.40), we simply combine the two equations in each subsystem to get the following four equations

$$\begin{cases} \frac{a}{2\gamma\delta t}\phi_{11}^{n+1} + \frac{S_{1}}{\epsilon^{3}}\phi_{11}^{n+1} - \frac{S_{2}}{\epsilon}\Delta\phi_{11}^{n+1} + \epsilon S_{3}\Delta^{2}\phi_{11}^{n+1} = G_{1}, \\ \frac{a}{2\gamma\delta t}\phi_{12}^{n+1} + \frac{S_{1}}{\epsilon^{3}}\phi_{12}^{n+1} - \frac{S_{2}}{\epsilon}\Delta\phi_{12}^{n+1} + \epsilon S_{3}\Delta^{2}\phi_{12}^{n+1} = G_{2}, \\ \frac{a}{2\gamma\delta t}\phi_{21}^{n+1} + \frac{S_{1}}{\epsilon^{3}}\phi_{21}^{n+1} - \frac{S_{2}}{\epsilon}\Delta\phi_{21}^{n+1} + \epsilon S_{3}\Delta^{2}\phi_{21}^{n+1} = G_{3}, \\ \frac{a}{2\gamma\delta t}\phi_{22}^{n+1} + \frac{S_{1}}{\epsilon^{3}}\phi_{22}^{n+1} - \frac{S_{2}}{\epsilon}\Delta\phi_{22}^{n+1} + \epsilon S_{3}\Delta^{2}\phi_{22}^{n+1} = G_{4}, \end{cases}$$

$$(3.43)$$

where

$$\begin{cases} G_1 = \left(\frac{S_1}{\epsilon^3}\phi^* - \frac{S_2}{\epsilon}\Delta\phi^* + \epsilon S_3\Delta^2\phi^*\right) + \frac{b\phi^n - c\phi^{n-1}}{2\delta t}, \\ G_2 = G_4 = -\epsilon(H^* - \frac{1}{|\Omega|}\int\limits_{\Omega} H^*d\mathbf{x}), \quad G_3 = -(\mathbf{u}^* \cdot \nabla)\phi^*. \end{cases}$$

Note $G_2 = G_4$ implies $\phi_{12}^{n+1} = \phi_{22}^{n+1}$. One can easily solve the four independent equations in (3.43) to get $(\phi_{11}, \phi_{12}, \phi_{21}, \phi_{22})^{n+1}$.

Third, we rewrite (3.22) into the following form

$$U^{n+1} = \frac{1}{2} \int_{\Omega} H^* \phi^{n+1} d\mathbf{x} + G_5, \tag{3.44}$$

where $G_5 = \frac{1}{a}(bU^n - cU^{n-1}) - \frac{1}{2a}\int_{\Omega}H^*(b\phi^n - c\phi^{n-1})d\mathbf{x}$. Replacing U^{n+1} and ϕ^{n+1} using the split form given in (3.30), we get

$$U_1^{n+1} + Q^{n+1}U_2^{n+1} = \frac{1}{2} \int_{\Omega} H^*(\phi_1^{n+1} + Q^{n+1}\phi_2^{n+1}) d\mathbf{x} + G_5.$$
(3.45)

We split the above result according to Q^{n+1} to derive

$$\begin{cases}
U_1^{n+1} = \frac{1}{2} \int_{\Omega} H^* \phi_1^{n+1} d\mathbf{x} + G_5, \\
U_2^{n+1} = \frac{1}{2} \int_{\Omega} H^* \phi_2^{n+1} d\mathbf{x}.
\end{cases} (3.46)$$

Replacing $(\phi_1, \phi_2)^{n+1}$ with the split form given in (3.36), we get

$$\begin{cases} U_1^{n+1} = \frac{1}{2} \int_{\Omega} H^*(\phi_{11}^{n+1} + U_1^{n+1} \phi_{12}^{n+1}) d\mathbf{x} + G_5, \\ U_2^{n+1} = \frac{1}{2} \int_{\Omega} H^*(\phi_{21}^{n+1} + U_2^{n+1} \phi_{22}^{n+1}) d\mathbf{x}. \end{cases}$$
(3.47)

By applying the simple factorization for each equality in (3.47), we derive

$$\begin{cases}
U_1^{n+1} = \frac{\frac{1}{2} \int_{\Omega} H^* \phi_{11}^{n+1} d\mathbf{x} + G_5}{1 - \frac{1}{2} \int_{\Omega} H^* \phi_{12}^{n+1} d\mathbf{x}}, \\
U_2^{n+1} = \frac{\frac{1}{2} \int_{\Omega} H^* \phi_{21}^{n+1} d\mathbf{x}}{1 - \frac{1}{2} \int_{\Omega} H^* \phi_{22}^{n+1} d\mathbf{x}}.
\end{cases} (3.48)$$

We need to verify (3.48) is solvable by showing the denominator $1 - \frac{1}{2} \int_{\Omega} H^* \phi_{22}^{n+1} d\mathbf{x} \neq 0$ (note $\phi_{12}^{n+1} = \phi_{22}^{n+1}$). By taking the L^2 inner product of the fourth equation in (3.43) with ϕ_{22}^{n+1} , and using $\int_{\Omega} \phi_{22}^{n+1} d\mathbf{x} = 0$, we get

$$-\epsilon \int_{\Omega} H^* \phi_{22}^{n+1} = \frac{a}{2\gamma \delta t} \|\phi_{22}^{n+1}\|^2 + \frac{S_1}{\epsilon^3} \|\phi_{22}^{n+1}\|^2 + \frac{S_2}{\epsilon} \|\nabla \phi_{22}^{n+1}\|^2 + \epsilon S_3 \|\Delta \phi_{22}^{n+1}\|^2 \ge 0, \tag{3.49}$$

which implies (3.48) is solvable. After we get U_1^{n+1} and U_2^{n+1} from (3.48), we update $(\phi_1, \phi_2, \mu_1, \mu_2)^{n+1}$ from (3.36). Fourth, we use the nonlocal variable Q^{n+1} to split the velocity field $\tilde{\mathbf{u}}^{n+1}$ as the following form:

$$\tilde{\mathbf{u}}^{n+1} = \tilde{\mathbf{u}}_1^{n+1} + Q^{n+1} \tilde{\mathbf{u}}_2^{n+1}. \tag{3.50}$$

By replacing the variables $\tilde{\mathbf{u}}^{n+1}$ in (3.21), and then splitting the obtained equation according to Q^{n+1} , we arrive at a system that includes two linear elliptic sub-equations with constant coefficients as follows:

$$\begin{cases}
\frac{a}{2\delta t}\tilde{\mathbf{u}}_{1}^{n+1} - \nu \Delta \tilde{\mathbf{u}}_{1}^{n+1} = -\nabla p^{n} + \frac{b\mathbf{u}^{n} - c\mathbf{u}^{n-1}}{2\delta t}, \\
\frac{a}{2\delta t}\tilde{\mathbf{u}}_{2}^{n+1} - \nu \Delta \tilde{\mathbf{u}}_{2}^{n+1} = -(\mathbf{u}^{*} \cdot \nabla)\mathbf{u}^{*} + \lambda \mu^{*}\nabla \phi^{*}.
\end{cases} (3.51)$$

The two split variables $\tilde{\mathbf{u}}_1^{n+1}$, $\tilde{\mathbf{u}}_2^{n+1}$ follow the boundary conditions described in (3.26), i.e., they are either periodic or satisfy:

$$\tilde{\mathbf{u}}_{1}^{n+1}|_{\partial\Omega} = \tilde{\mathbf{u}}_{2}^{n+1}|_{\partial\Omega} = \mathbf{0}. \tag{3.52}$$

Fifth, we solve the auxiliary variable Q^{n+1} . Using the split form for the variables $\tilde{\mathbf{u}}^{n+1}$ in (3.50) and μ^{n+1} in (3.30), one can rewrite the scheme (3.23) as the following form:

$$(\frac{a}{2\delta t} - \vartheta_2)Q^{n+1} = \frac{1}{2\delta t}(bQ^n - cQ^{n-1}) + \vartheta_1, \tag{3.53}$$

where

$$\begin{cases} \vartheta_{1} = \int\limits_{\Omega} \left(\lambda(\mathbf{u}^{*} \cdot \nabla) \phi^{*} \mu_{1}^{n+1} - \lambda \mu^{*} \nabla \phi^{*} \cdot \tilde{\mathbf{u}}_{1}^{n+1} + (\mathbf{u}^{*} \cdot \nabla) \mathbf{u}^{*} \cdot \tilde{\mathbf{u}}_{1}^{n+1} \right) d\mathbf{x}, \\ \vartheta_{2} = \int\limits_{\Omega} \left(\lambda(\mathbf{u}^{*} \cdot \nabla) \phi^{*} \mu_{2}^{n+1} - \lambda \mu^{*} \nabla \phi^{*} \cdot \tilde{\mathbf{u}}_{2}^{n+1} + (\mathbf{u}^{*} \cdot \nabla) \mathbf{u}^{*} \cdot \tilde{\mathbf{u}}_{2}^{n+1} \right) d\mathbf{x}. \end{cases}$$

$$(3.54)$$

We need to verify the solvability of (3.53) by showing $\frac{a}{2\delta t} - \vartheta_2 \neq 0$ as follows. By multiplying the L^2 inner product of the second equation in (3.51) with $\tilde{\mathbf{u}}_2^{n+1}$, we get

$$\int_{\Omega} \left(-(\mathbf{u}^* \cdot \nabla) \mathbf{u}^* \cdot \tilde{\mathbf{u}}_2^{n+1} + \lambda \mu^* \nabla \phi^* \cdot \tilde{\mathbf{u}}_2^{n+1} \right) d\mathbf{x} = \frac{a}{2\delta t} \|\tilde{\mathbf{u}}_2^{n+1}\|^2 + \nu \|\nabla \tilde{\mathbf{u}}_2^{n+1}\|^2 \ge 0.$$
(3.55)

By taking the L^2 inner product of the first equation in (3.33) with $\lambda \mu_2^{n+1}$, of the second equation with $-\lambda \frac{a}{2\delta t}\phi_2^{n+1}$, and combining the two obtained equations, we derive

$$-\int_{\Omega} \lambda(\mathbf{u}^{*} \cdot \nabla) \phi^{*} \mu_{2}^{n+1} d\mathbf{x} = \lambda \gamma \left\| \mu_{2}^{n+1} - \frac{1}{|\Omega|} \int_{\Omega} \mu_{2}^{n+1} d\mathbf{x} \right\|^{2} + \frac{a\lambda}{2\delta t} \left(\frac{S_{1}}{\epsilon^{3}} \|\phi_{2}^{n+1}\|^{2} + \frac{S_{2}}{\epsilon} \|\nabla \phi_{2}^{n+1}\|^{2} + \epsilon S_{3} \|\Delta \phi_{2}^{n+1}\|^{2} \right) + \frac{a\lambda \epsilon}{2\delta t} U_{2}^{n+1} \int_{\Omega} H^{*} \phi_{2}^{n+1} d\mathbf{x}.$$
(3.56)

From the second equation in (3.46), we derive

$$U_2^{n+1} \int_{\Omega} H^* \phi_2^{n+1} d\mathbf{x} = \frac{1}{2} \left(\int_{\Omega} H^* \phi_2^{n+1} d\mathbf{x} \right)^2, \tag{3.57}$$

which implies

$$-\int_{\Omega} \lambda(\mathbf{u}^* \cdot \nabla) \phi^* \mu_2^{n+1} d\mathbf{x} \ge 0. \tag{3.58}$$

Therefore, from (3.55) and (3.56), we derive $-\vartheta_2 \ge 0$, and the solvability of (3.53) is then verified. Finally, we update ϕ^{n+1} , μ^{n+1} , U^{n+1} from (3.30), $\tilde{\mathbf{u}}^{n+1}$ from (3.50), and obtain \mathbf{u}^{n+1} , p^{n+1} from (3.24)-(3.25) using the process described in Remark 3.3.

In summary, the scheme (3.19)-(3.25) can be implemented in the following way:

- *Stage 1*: Compute $(\phi_{11}, \phi_{12}, \phi_{21}, \phi_{22})^{n+1}$ from (3.43); *Stage 2*: Update $(U_1, U_2)^{n+1}$ from (3.48);
- *Stage* 3: Update $(\phi_1, \phi_2, \mu_1, \mu_2)^{n+1}$ from (3.36);
- Stage 4: Compute $(\tilde{\mathbf{u}}_1, \tilde{\mathbf{u}}_2)^{n+1}$ from (3.51);
- Stage 5: Compute Q^{n+1} from (3.53);
- Stage 6: Update ϕ^{n+1} , μ^{n+1} , U^{n+1} from (3.30), and $\tilde{\mathbf{u}}^{n+1}$ from (3.50);
- Stage 7: Compute \mathbf{u}^{n+1} and p^{n+1} from (3.24)-(3.25) using the process described in Remark 3.3.

Hence, the total cost of solving the scheme (3.19)-(3.25) at each time step includes solving three independent biharmonic equations in Stage 1 (note $\phi_{12}^{n+1} = \phi_{22}^{n+1}$), two elliptic type equations in Stage 4, and one Poisson type equation in Step 7. All these equations have constant coefficients and are completely decoupled, which means very effective calculations in practice.

3.4. Unconditional energy stability

The following theorem ensures that the developed scheme (3.19)-(3.25) satisfies the energy stability unconditionally.

Theorem 3.1. The following discrete energy dissipation law holds for the scheme (3.19)-(3.25),

$$\frac{1}{\delta t}(E^{n+1} - E^{n-1}) \le -\nu \|\nabla \tilde{\mathbf{u}}^{n+1}\|^2 - \lambda \gamma \left\| \mu^{n+1} - \frac{1}{|\Omega|} \int_{\Omega} \mu^{n+1} d\mathbf{x} \right\|^2 \le 0, \tag{3.59}$$

where

$$E^{n+1} = \frac{1}{2} \left(\frac{1}{2} \| \mathbf{u}^{n+1} \|^2 + \frac{1}{2} \| 2\mathbf{u}^{n+1} - \mathbf{u}^n \|^2 \right) + \frac{\delta t^2}{3} \| \nabla p^{n+1} \|^2$$

$$+ \lambda \epsilon \left(\frac{1}{2} |U^{n+1}|^2 + \frac{1}{2} |2U^{n+1} - U^n|^2 \right) + \frac{1}{2} \left(\frac{1}{2} |Q^{n+1}|^2 + \frac{1}{2} |2Q^{n+1} - Q^n|^2 \right)$$

$$+ \frac{1}{2} \lambda \frac{S_1}{\epsilon^3} \| \phi^{n+1} - \phi^n \|^2 + \frac{1}{2} \lambda \frac{S_2}{\epsilon} \| \nabla (\phi^{n+1} - \phi^n) \|^2 + \frac{1}{2} \lambda \epsilon S_3 \| \Delta (\phi^{n+1} - \phi^n) \|^2.$$

$$(3.60)$$

Proof. We multiply the inner product of (3.21) with $2\delta t \tilde{\mathbf{u}}^{n+1}$ in the L^2 space, we obtain

$$(3\tilde{\mathbf{u}}^{n+1} - 4\mathbf{u}^n + \mathbf{u}^{n-1}, \tilde{\mathbf{u}}^{n+1}) + 2\nu\delta t \|\nabla \tilde{\mathbf{u}}^{n+1}\|^2 + 2\delta t (\nabla p^n, \tilde{\mathbf{u}}^{n+1})$$

$$= -2\delta t Q^{n+1} \int_{\Omega} (\mathbf{u}^* \cdot \nabla) \mathbf{u}^* \cdot \tilde{\mathbf{u}}^{n+1} d\mathbf{x} + 2\delta t \lambda Q^{n+1} \int_{\Omega} \mu^* \nabla \phi^* \cdot \tilde{\mathbf{u}}^{n+1} d\mathbf{x}.$$
(3.61)

From (3.24), for any variable \mathbf{v} with $\nabla \cdot \mathbf{v} = 0$, we have

$$(\mathbf{u}^{n+1}, \mathbf{v}) = (\tilde{\mathbf{u}}^{n+1}, \mathbf{v}). \tag{3.62}$$

We derive following equality

$$(3\tilde{\mathbf{u}}^{n+1} - 4\mathbf{u}^{n} + \mathbf{u}^{n-1}, \tilde{\mathbf{u}}^{n+1})$$

$$= (3\tilde{\mathbf{u}}^{n+1} - 4\mathbf{u}^{n} + \mathbf{u}^{n-1}, \mathbf{u}^{n+1}) + (3\tilde{\mathbf{u}}^{n+1} - 4\mathbf{u}^{n} + \mathbf{u}^{n-1}, \tilde{\mathbf{u}}^{n+1} - \mathbf{u}^{n+1})$$

$$= (3\mathbf{u}^{n+1} - 4\mathbf{u}^{n} + \mathbf{u}^{n-1}, \mathbf{u}^{n+1}) + (3\tilde{\mathbf{u}}^{n+1}, \tilde{\mathbf{u}}^{n+1} - \mathbf{u}^{n+1})$$

$$= (3\mathbf{u}^{n+1} - 4\mathbf{u}^{n} + \mathbf{u}^{n-1}, \mathbf{u}^{n+1}) + 3(\tilde{\mathbf{u}}^{n+1} - \mathbf{u}^{n+1}, \tilde{\mathbf{u}}^{n+1} + \mathbf{u}^{n+1})$$

$$= \frac{1}{2} \left(\|\mathbf{u}^{n+1}\|^{2} - \|\mathbf{u}^{n}\|^{2} + \|2\mathbf{u}^{n+1} - \mathbf{u}^{n}\|^{2} - \|2\mathbf{u}^{n} - \mathbf{u}^{n-1}\|^{2} + \|\mathbf{u}^{n+1} - 2\mathbf{u}^{n} + \mathbf{u}^{n-1}\|^{2} \right) + 3(\|\tilde{\mathbf{u}}^{n+1}\|^{2} - \|\mathbf{u}^{n+1}\|^{2}),$$

$$(3.63)$$

where we use the following identity

$$2(3a - 4b + c, a) = a^{2} - b^{2} + (2a - b)^{2} - (2b - c)^{2} + (a - 2b + c)^{2}.$$
(3.64)

We reformulate the projection step (3.24) as

$$\frac{3}{2\delta t}\mathbf{u}^{n+1} + \nabla p^{n+1} = \frac{3}{2\delta t}\tilde{\mathbf{u}}^{n+1} + \nabla p^n. \tag{3.65}$$

By taking the square of both sides of the above equation, we get

$$\frac{9}{4\delta t^2} \|\mathbf{u}^{n+1}\|^2 + \|\nabla p^{n+1}\|^2 = \frac{9}{4\delta t^2} \|\tilde{\mathbf{u}}^{n+1}\|^2 + \|\nabla p^n\|^2 + \frac{3}{\delta t} (\tilde{\mathbf{u}}^{n+1}, \nabla p^n). \tag{3.66}$$

Hence, by multiplying $2\delta t^2/3$ of the above equation, we derive

$$\frac{3}{2}(\|\mathbf{u}^{n+1}\|^2 - \|\tilde{\mathbf{u}}^{n+1}\|^2) + \frac{2\delta t^2}{3}(\|\nabla p^{n+1}\|^2 - \|\nabla p^n\|^2) = 2\delta t(\tilde{\mathbf{u}}^{n+1}, \nabla p^n). \tag{3.67}$$

By taking the inner product of (3.24) with $2\delta t \mathbf{u}^{n+1}$ in the L^2 space, we have

$$\frac{3}{2}(\|\mathbf{u}^{n+1}\|^2 - \|\tilde{\mathbf{u}}^{n+1}\|^2 + \|\mathbf{u}^{n+1} - \tilde{\mathbf{u}}^{n+1}\|^2) = 0.$$
(3.68)

We combine (3.61), (3.63), (3.67), and (3.68) to obtain

$$\frac{1}{2}(\|\mathbf{u}^{n+1}\|^{2} - \|\mathbf{u}^{n}\|^{2} + \|2\mathbf{u}^{n+1} - \mathbf{u}^{n}\|^{2} - \|2\mathbf{u}^{n} - \mathbf{u}^{n-1}\|^{2} + \|\mathbf{u}^{n+1} - 2\mathbf{u}^{n} + \mathbf{u}^{n-1}\|^{2})
+ \frac{3}{2}\|\mathbf{u}^{n+1} - \tilde{\mathbf{u}}^{n+1}\|^{2} + \frac{2\delta t^{2}}{3}(\|\nabla p^{n+1}\|^{2} - \|\nabla p^{n}\|^{2}) + 2\nu\delta t\|\nabla \tilde{\mathbf{u}}^{n+1}\|^{2}
= -2\delta t Q^{n+1} \int_{\Omega} (\mathbf{u}^{*} \cdot \nabla)\mathbf{u}^{*} \cdot \tilde{\mathbf{u}}^{n+1} d\mathbf{x} + 2\delta t\lambda Q^{n+1} \int_{\Omega} (\mu^{*} \nabla \phi^{*}) \cdot \tilde{\mathbf{u}}^{n+1} d\mathbf{x}.$$
(3.69)

Computing the inner product of (3.19) with $2\lambda\delta t\mu^{n+1}$ in the L^2 space, we have

$$\lambda(3\phi^{n+1} - 4\phi^n + \phi^{n-1}, \mu^{n+1}) + 2\lambda\gamma\delta t \left\| \mu^{n+1} - \frac{1}{|\Omega|} \int_{\Omega} \mu^{n+1} d\boldsymbol{x} \right\|^2$$

$$= -2\lambda\delta t Q^{n+1} \int_{\Omega} (\mathbf{u}^* \cdot \nabla)\phi^* \mu^{n+1} d\boldsymbol{x}.$$
(3.70)

Computing the L^2 inner product of (3.20) with $-\lambda(3\phi^{n+1}-4\phi^n+\phi^{n-1})$, we find

$$-\lambda(\mu^{n+1}, 3\phi^{n+1} - 4\phi^{n} + \phi^{n-1}) + \lambda \frac{S_{1}}{\epsilon^{3}}(\phi^{n+1} - \phi^{*}, 3\phi^{n+1} - 4\phi^{n} + \phi^{n-1})$$

$$+\lambda \frac{S_{2}}{\epsilon}(\nabla(\phi^{n+1} - \phi^{*}), \nabla(3\phi^{n+1} - 4\phi^{n} + \phi^{n-1}))$$

$$+\lambda \epsilon S_{3}(\Delta(\phi^{n+1} - \phi^{*}), \Delta(3\phi^{n+1} - 4\phi^{n} + \phi^{n-1}))$$

$$= -\epsilon \lambda U^{n+1} \int_{\Omega} H^{*}(3\phi^{n+1} - 4\phi^{n} + \phi^{n-1}) d\mathbf{x}.$$

$$(3.71)$$

By multiplying (3.22) with $2\lambda \epsilon U^{n+1}$ and using (3.64), we obtain

$$\lambda \epsilon (|U^{n+1}|^2 - |U^n|^2 + |2U^{n+1} - U^n|^2 - |2U^n - U^{n-1}|^2 + |U^{n+1} - 2U^n + U^{n-1}|^2)$$

$$= \epsilon \lambda U^{n+1} \int_{\Omega} H^* (3\phi^{n+1} - 4\phi^n + \phi^{n-1}) d\mathbf{x}.$$
(3.72)

By multiplying (3.23) with $2\delta t Q^{n+1}$ and using (3.64), we obtain

$$\frac{1}{2} \Big(|Q^{n+1}|^2 - |Q^n|^2 + |2Q^{n+1} - Q^n|^2 - |2Q^n - Q^{n-1}|^2 + |Q^{n+1} - 2Q^n + Q^{n-1}|^2 \Big)
= 2\lambda \delta t Q^{n+1} \int_{\Omega} (\mathbf{u}^* \cdot \nabla) \phi^* \mu^{n+1} - 2\lambda \delta t Q^{n+1} \int_{\Omega} (\mu^* \nabla \phi^*) \cdot \tilde{\mathbf{u}}^{n+1} d\mathbf{x}
+ 2\delta t Q^{n+1} \int_{\Omega} (\mathbf{u}^* \cdot \nabla) \mathbf{u}^* \cdot \tilde{\mathbf{u}}^{n+1} d\mathbf{x}.$$
(3.73)

Hence, by combining (3.69)-(3.73), we arrive at

$$\begin{split} &\frac{1}{2}(\|\mathbf{u}^{n+1}\|^2 - \|\mathbf{u}^n\|^2 + \|2\mathbf{u}^{n+1} - \mathbf{u}^n\|^2 - \|2\mathbf{u}^n - \mathbf{u}^{n-1}\|^2) + \frac{2\delta t^2}{3}(\|\nabla p^{n+1}\|^2 - \|\nabla p^n\|^2) \\ &\quad + \lambda \frac{S_1}{\epsilon^3}(\|\phi^{n+1} - \phi^n\|^2 - \|\phi^n - \phi^{n-1}\|^2) + \lambda \frac{S_2}{\epsilon}(\|\nabla \phi^{n+1} - \nabla \phi^n\|^2 - \|\nabla \phi^n - \nabla \phi^{n-1}\|^2) \\ &\quad + \lambda \epsilon S_3(\|\Delta (\phi^{n+1} - \phi^n)\|^2 - \|\Delta (\phi^n - \phi^{n-1})\|^2) \\ &\quad + \lambda \epsilon (|U^{n+1}|^2 - |U^n|^2 + |2U^{n+1} - U^n|^2 - |2U^n - U^{n-1}|^2) \\ &\quad + \frac{1}{2}(|Q^{n+1}|^2 - |Q^n|^2 + |2Q^{n+1} - Q^n|^2 - |2Q^n - Q^{n-1}|^2) \\ &\quad + \left\{ \frac{1}{2}\|\mathbf{u}^{n+1} - 2\mathbf{u}^n + \mathbf{u}^{n-1}\|^2 + \frac{3}{2}\|\mathbf{u}^{n+1} - \tilde{\mathbf{u}}^{n+1}\|^2 \\ &\quad + 2\lambda \frac{S_1}{\epsilon^3}\|\phi^{n+1} - 2\phi^n + \phi^{n-1}\|^2 + 2\lambda \frac{S_2}{\epsilon}\|\nabla (\phi^{n+1} - 2\phi^n + \phi^{n-1})\|^2 \\ &\quad + 2\lambda \epsilon S_3\|\Delta (\phi^{n+1} - 2\phi^n + \phi^{n-1})\|^2 \\ &\quad + \lambda \epsilon |U^{n+1} - 2U^n + U^{n-1}|^2 + \frac{1}{2}|Q^{n+1} - 2Q^n + Q^{n-1}|^2 \right\} \\ &= -2\delta t \nu \|\nabla \tilde{\mathbf{u}}^{n+1}\|^2 - 2\delta t \lambda \gamma \left\|\mu^{n+1} - \frac{1}{|\Omega|}\int \mu^{n+1} d\mathbf{x} \right\|^2, \end{split}$$

where we use the following identity:

$$(3a - 4b + c)(a - 2b + c) = (a - b)^{2} - (b - c)^{2} + 2(a - 2b + c)^{2}.$$
(3.75)

Finally, we obtain (3.59) from (3.74) after dropping the positive terms in $\{\}$ and dividing both sides by 2. \square

4. Numerical simulations

In this section, we use numerical examples to verify the accuracy and energy stability of the proposed fully-decoupled scheme using scalar auxiliary variables (3.19)-(3.25) (referred to as DSAV for short). Numerical simulations include accuracy/stability tests, multiple vesicle deformation in 2D and 3D, as well as a rising vesicle under the action of gravity force in 2D and 3D. In all numerical examples, we set the computational domain to be rectangular. For directions with periodic

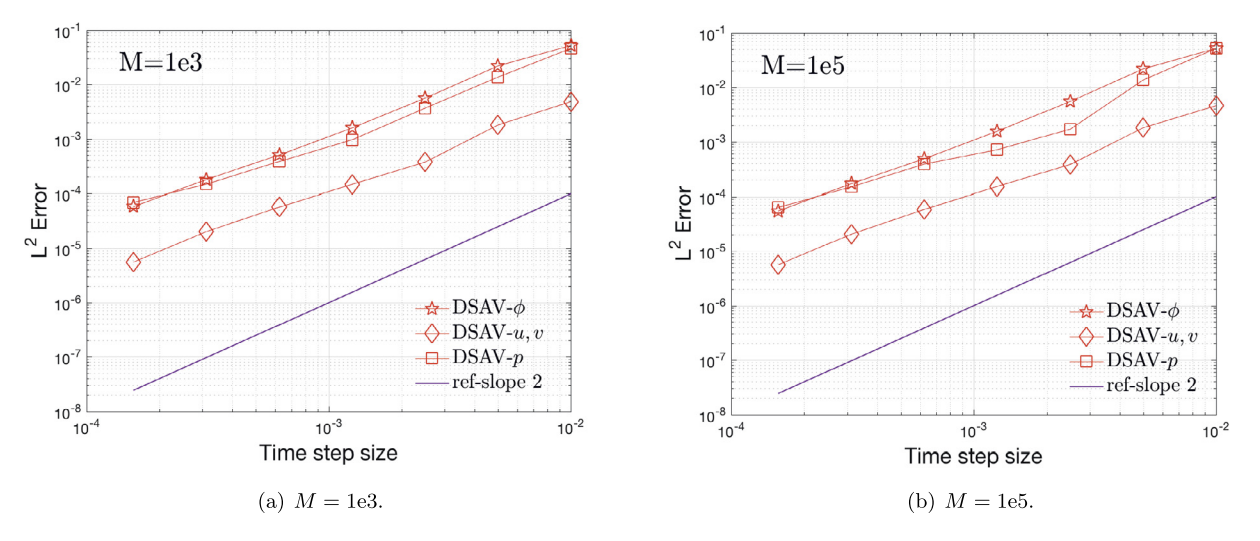


Fig. 4.1. Accuracy tests. The numerical errors in L^2 for all variables computed by using the scheme DSAV with different time steps, where two surface area parameters are used, (a) M = 1e3, and (b) M = 1e5. (For the velocity field $\mathbf{u} = (u, v)$, we plot the mean of the errors of the two velocity components.)

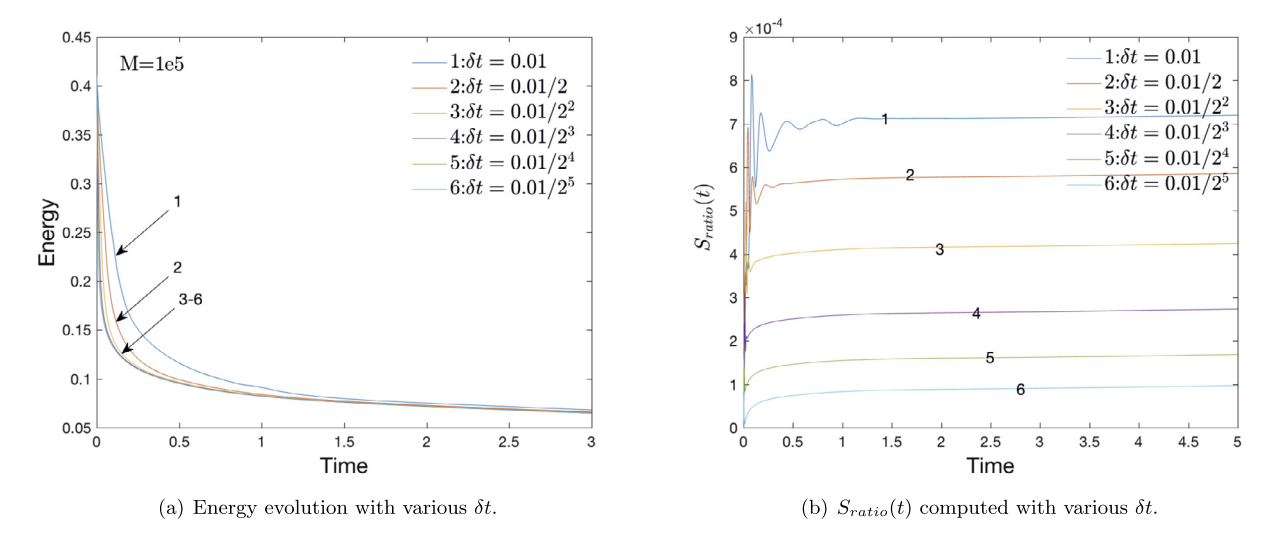


Fig. 4.2. Stability tests. (a) The time evolution curves of the total free energy (2.1) calculated by the scheme DSAV with different time steps, where the surface area parameter is M = 1e5. (b) Time evolution curves of $S_{ratio}(t)$ computed with various time steps. (For interpretation of the colors in the figure(s), the reader is referred to the web version of this article.)

boundary conditions, the Fourier-spectral method is used for discretization. For directions with boundary conditions specified in (3.26), the Legendre-Galerkin method is adopted for discretization, where the inf-sup stable pair (P_N, P_{N-2}) is used for the velocity $(\tilde{\mathbf{u}} \text{ and } \mathbf{u})$ and pressure p, respectively, and P_N is used for variables ϕ , μ .

4.1. Accuracy and stability tests

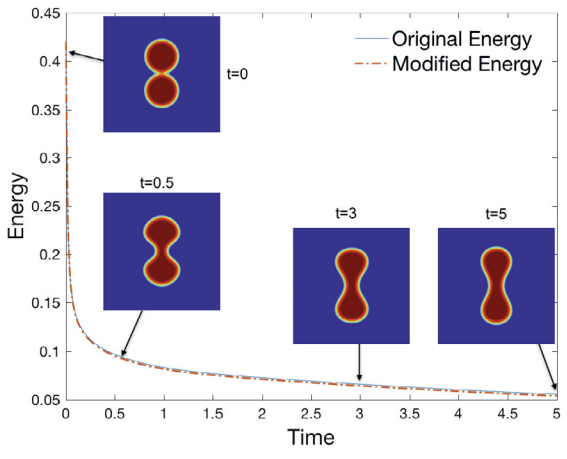
We perform the convergence tests by refining the time step. We set the 2D domain as $(x, y) \in \Omega = [0, 2\pi]^2$ and assume the periodic boundary conditions where 129 Fourier modes are used for each direction, so the error in spatial directions can be ignored. We set the model parameters as

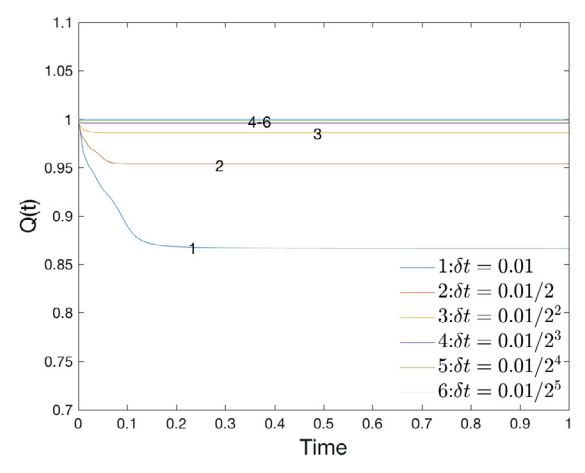
$$\epsilon = 0.07, \nu = 1, \gamma = 0.1, B = 1, S_1 = 4, S_2 = 4, S_3 = 1, \lambda = 0.01,$$
 (4.1)

and assume the initial condition as follows (the profile of ϕ is shown in Fig. 4.3(a)),

$$\phi(x,y)|_{t=0} = \sum_{i=1}^{2} \tanh\left(\frac{r - \sqrt{(x - x_i)^2 + (y - y_i)^2}}{\sqrt{2}\epsilon}\right) + 1, \mathbf{u}(x,y) = \mathbf{0}, p^0 = 0,$$
(4.2)

where $r = 0.28\pi$, $(x_1, x_2) = (\pi, \pi)$, $(y_1, y_2) = (1.29\pi, -1.29\pi)$.





(a) Time evolution of the original and modified energy.

(b) Time evolution of Q(t) with various δt .

t = 5

Fig. 4.3. (a) The time evolution curves of the original total free energy (2.1) and the modified energy (3.60) calculated by the developed scheme DSAV with $\delta t = \frac{0.01}{2^3}$ for M = 1e5 (snapshots of ϕ at various times are superimposed). (b) The time evolution of the auxiliary variable Q(t) over time using different time steps.

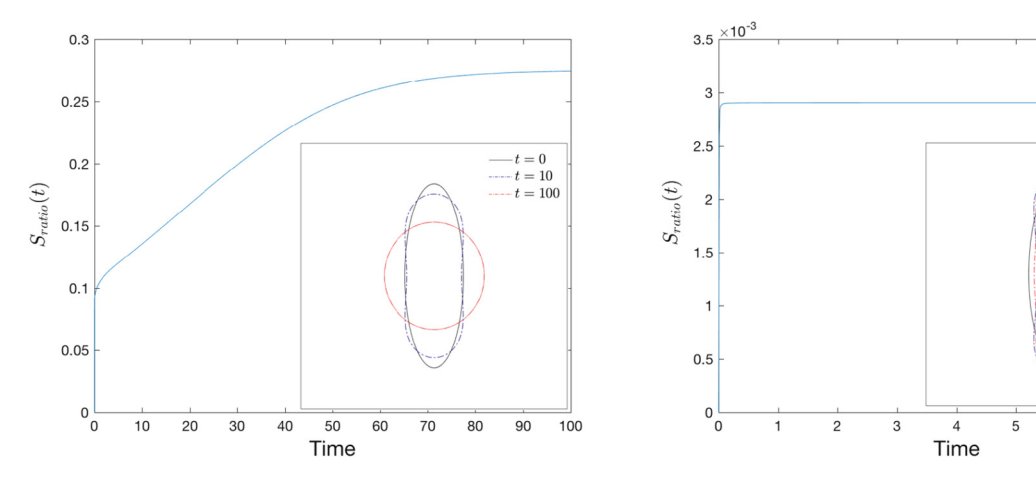


Fig. 4.4. Time evolution of $S_{ratio}(t)$, where two penalty parameters are used: (a) M = 0 and (b) M = 1e5. In each figure, the interface contour of ϕ at different times are plotted in the small inset subfigure. (Example 4.2.1: deformation of a 2D narrow elliptical vesicle.)

We compute the L^2 error of the variables ϕ , \mathbf{u} , p when t=0.2. Since the exact solution is not yet known, the numerical solution calculated by DSAV with a small time step $\delta t=1e-8$ is used as an approximate exact solution. We change the time step from 0.01 to $0.01/2^6$ with a factor of 1/2 for each computation. The convergence rate of DSAV is shown in Fig. 4.1 (a)-(b), where two different surface area penalty parameters M=1e3 and M=1e5 are used. We find that the scheme DSAV always shows second-order accuracy for all cases and all variables.

Next, we perform energy stability tests using different time steps. In Fig. 4.2 (a), we plot six energy evolution curves calculated using DSAV, with time steps ranging from $\delta t = 0.01$ to $0.01/2^5$ with a factor of 1/2. All the obtained curves display very good monotonic attenuation. In Fig. 4.2 (b), we plot the time evolution of the function $S_{ratio}(t) := \frac{|A(\phi(t)) - A(\phi^0)|}{A(\phi^0)}$ (ratio of the surface area difference) computed using different time steps. It can be seen that the surface area variation is around the scale of 9e - 4. When the time step is relatively small, S_{ratio} becomes smaller, indicating that the scheme is more accurate. In Fig. 4.3 (a), using the time step $\delta t = \frac{0.01}{2^3}$, we plot the evolution curve of original energy (2.1) and the modified energy (3.60) with time. We find that the two energies match very well. Meanwhile, we attach the profiles of the phase variable ϕ at different times in the figure. It can be seen that the two vesicles, which were very close at the initial moment, eventually become a steady capsule shape with a thinner center and thicker ends. In Fig. 4.3 (b), we plot the evolution of the auxiliary variable Q with time. When the time step is small, Q is very close to 1.

4.2. Deformation of stacked vesicles in 2D and 3D

In the following examples, we set the initial condition to one or more stacked vesicles with different shapes to study their dynamical topological changes, including the fusion of multiple stacked vesicles, and the shape change caused the shear

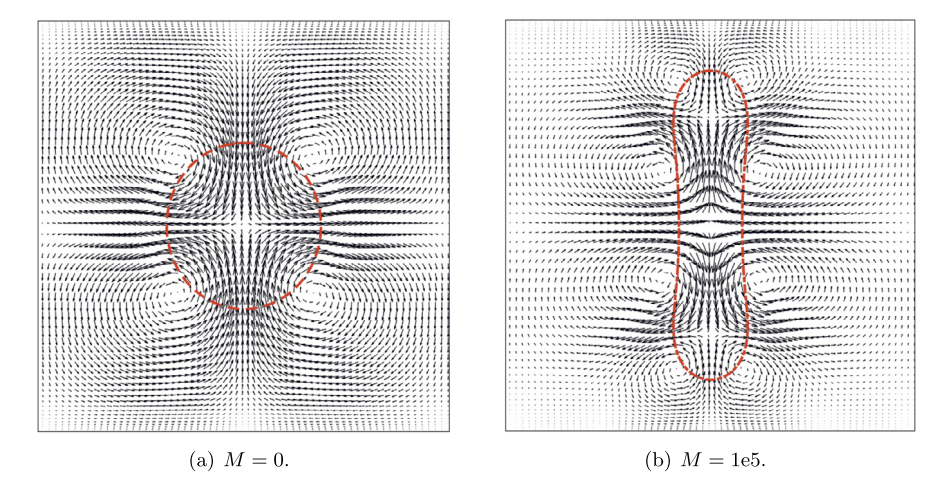


Fig. 4.5. The velocity field of the final equilibrium solutions, which is superimposed by the interface contour of the phase-field variable ϕ , where (a) M = 0 and (b) M = 1e5. (Example 4.2.1: deformation of a 2D narrow elliptical vesicle).

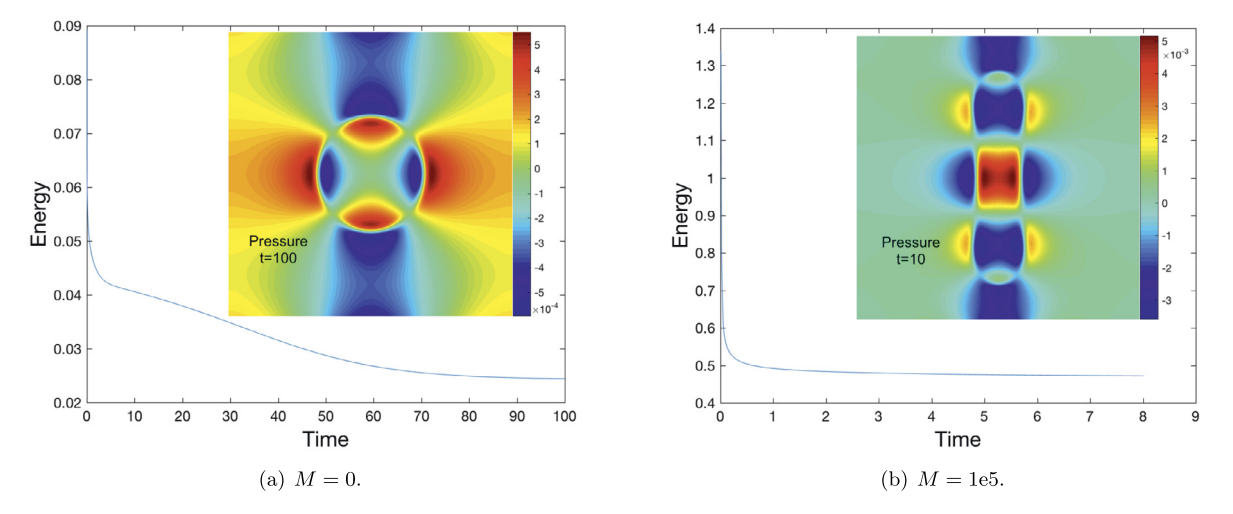


Fig. 4.6. Time evolution of the total free energy (3.60) with (a) M = 0 and (b) M = 1e5. In each figure, the color graph of the pressure p at the steady state is plotted in the small inset subfigure. (Example 4.2.1: deformation of a 2D narrow elliptical vesicle).

flow on the boundary. For all 2D simulations, we use rectangular region $(x, y) \in \Omega = [0, L_1] \times [0, L_2]$, where the x direction is assumed to satisfy periodic boundary conditions, and the y direction is assumed to be non-periodic boundary conditions (3.26). For all 3D simulations, the computational domain is set to $(x, y, z) \in \Omega = [0, L_1] \times [0, L_2] \times [0, L_3]$, where the x and y directions are assumed to satisfy periodic boundary conditions, and the z direction is assumed to be non-periodic boundary conditions (3.26). For the direction with periodic boundary conditions, we adopt the Fourier spectral method for discretization, and for the direction with non-periodic boundary conditions (3.26), we adopt the Legendre-Galerkin method for spatial discretization.

4.2.1. Deformation of a narrow 2D elliptical vesicle

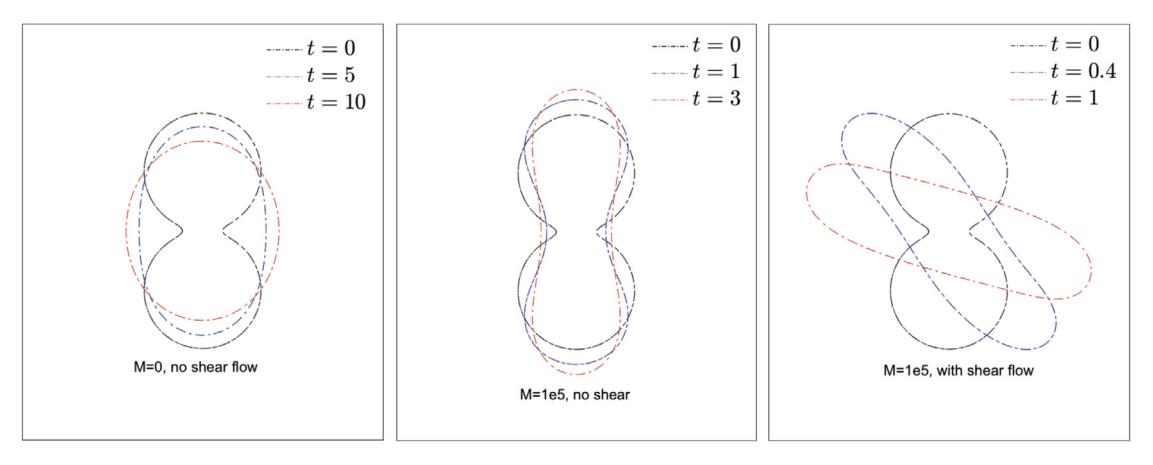
In this example, we set the initial shape of the vesicle to be a narrow ellipse to study its deformation the final equilibrium shape under different surface area parameter M. We set the computational domain to $\Omega = [0, 2\pi]^2$, and the initial conditions are set as

$$\phi(x,y)|_{t=0} = \tanh\left(\frac{0.4\pi - \sqrt{(x-\pi)^2/0.3 + (y-\pi)^2/3}}{\sqrt{2}\epsilon}\right), \mathbf{u}(x,y) = \mathbf{0}, p^0 = 0.$$
(4.3)

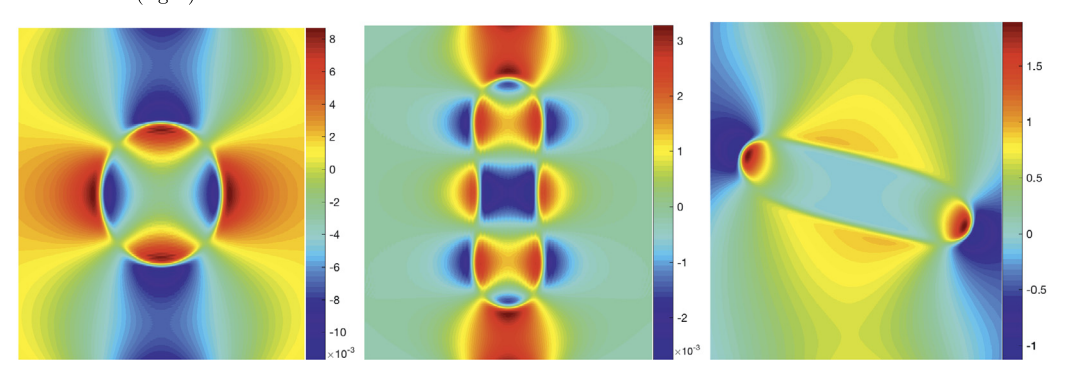
The following model parameters are used:

$$\epsilon = 0.1, \nu = 1, \gamma = 0.1, B = 1, S_1 = 4, S_2 = 4, S_3 = 1, \lambda = 0.01, \delta t = 1e - 3.$$
 (4.4)

We adopt 257 Fourier modes to discretize the *x* direction, and the Legendre polynomial up to the degree of 256 to discretize the *y* direction.



(a) Interface contour with M=0 (left), M=1e5 without shear (middle), and M=1e5 with shear (right).



(b) The pressure p with M=0 (left), M=1e5 without shear (middle), and M=1e5 with shear (right).

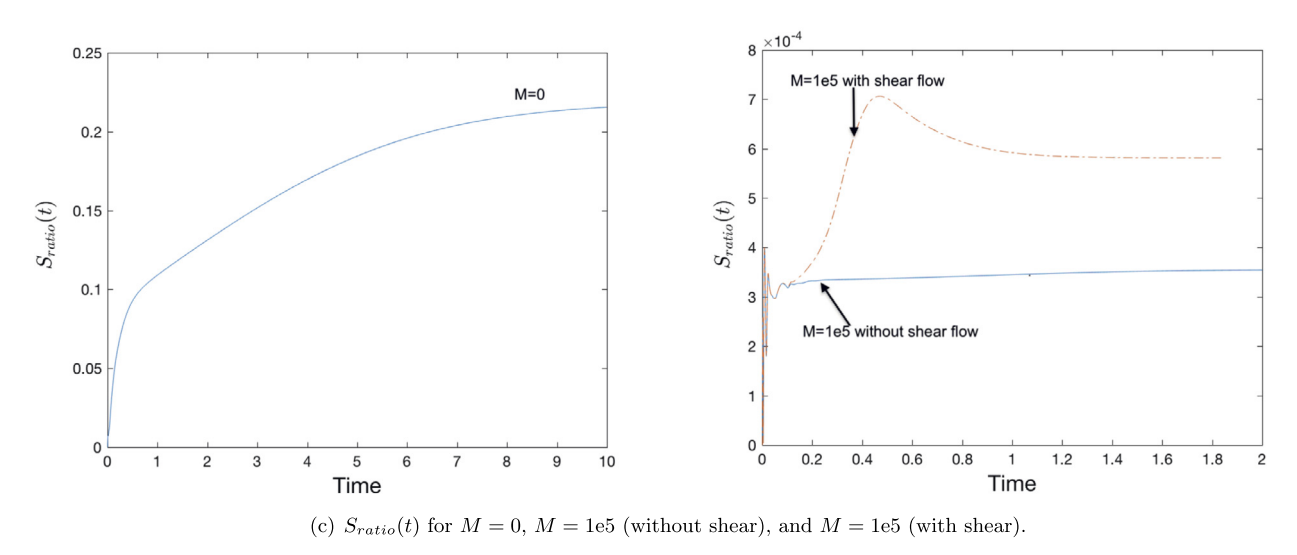


Fig. 4.7. Deformations of two 2D stacked circular vesicles (Example 4.2.2) where (a) interface contour of ϕ with M=0, M=1e5 (without shear), and M=1e5 (with shear); (b) color plots of steady-state pressure p; and (c) time evolution of $S_{ratio}(t)$ for these three cases.

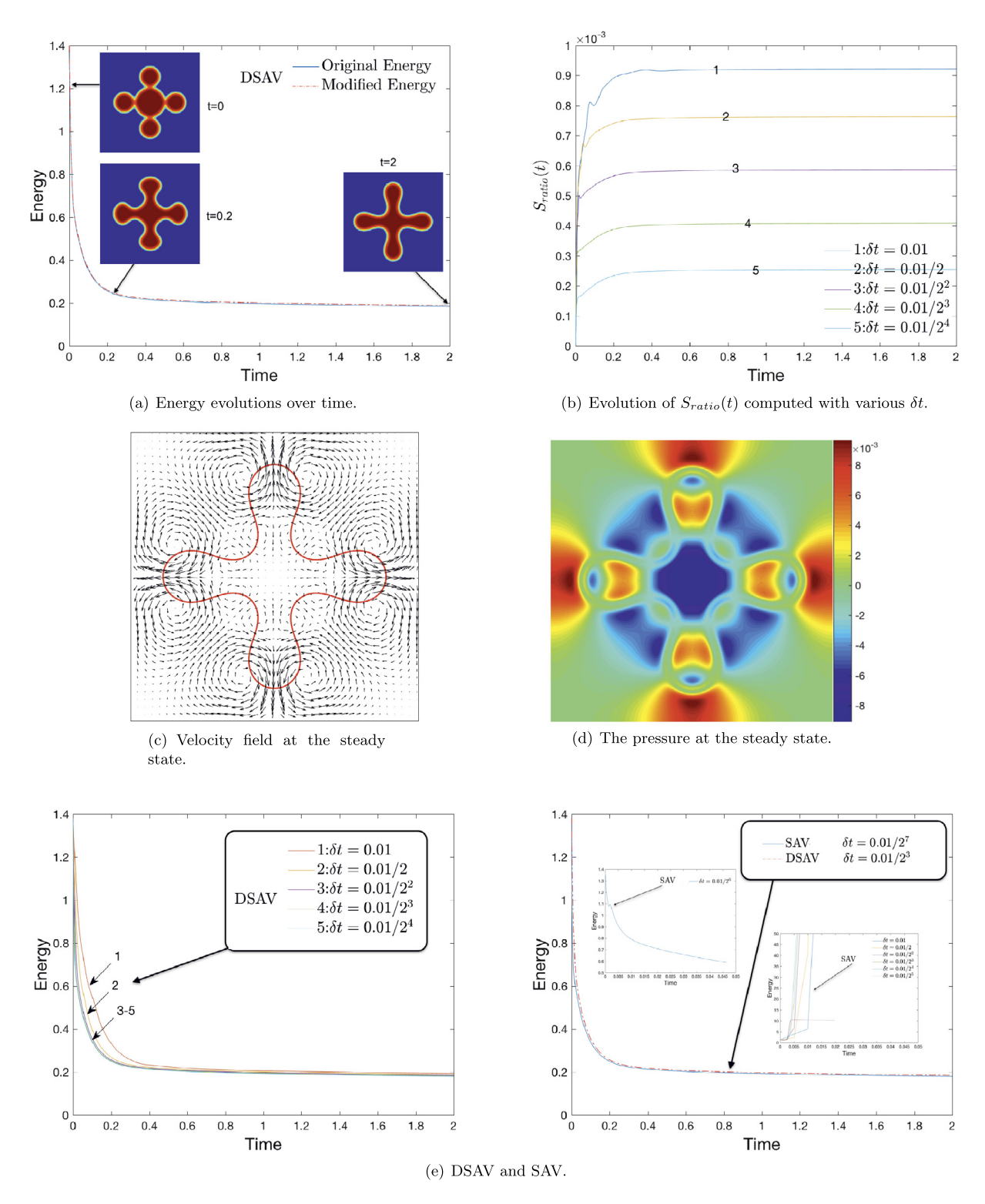


Fig. 4.8. The deformation of five 2D stacked circular vesicles (Example 4.2.3) where (a) energy evolution curves superimposed with ϕ at different times; (b) time evolution of $S_{ratio}(t)$ computed by using various time steps; (c) the velocity field at the steady state; (d) the pressure p at the stead state; and (e) energy evolution curves computed by using schemes DSAV and SAV with various time steps.

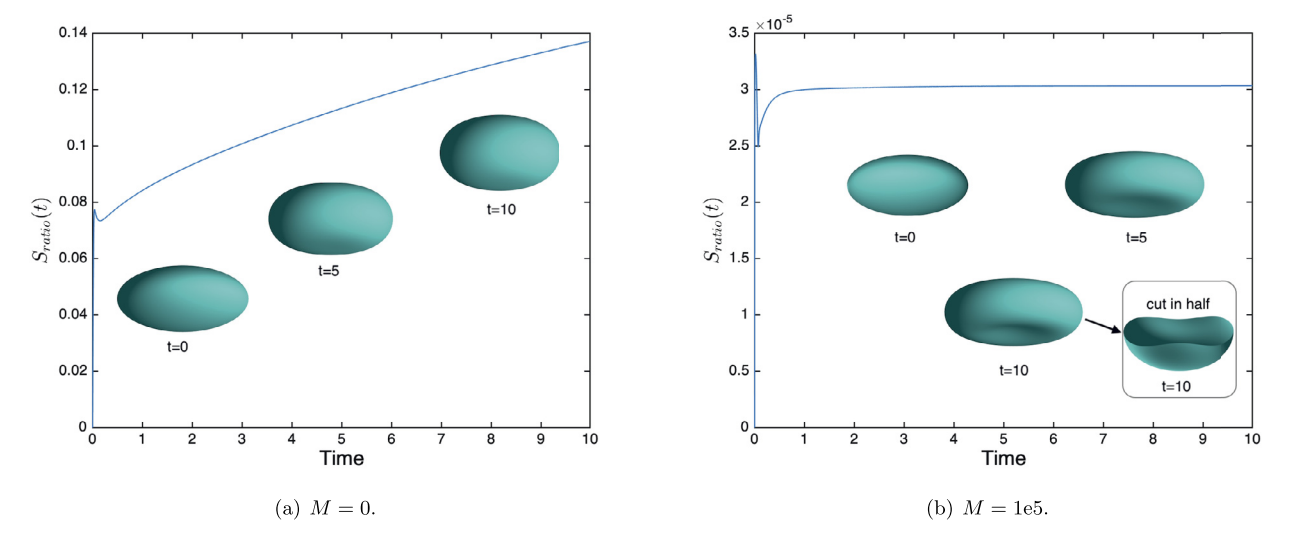


Fig. 4.9. Deformations of a wide ellipsoid vesicle (Example 4.2.4) using two surface area parameters where (a) M=0 and (b) M=1e5. In each subfigure, we plot $S_{ratio}(t)$ with time, which is superimposed by the isosurface of $\{\phi=0\}$ at different times.

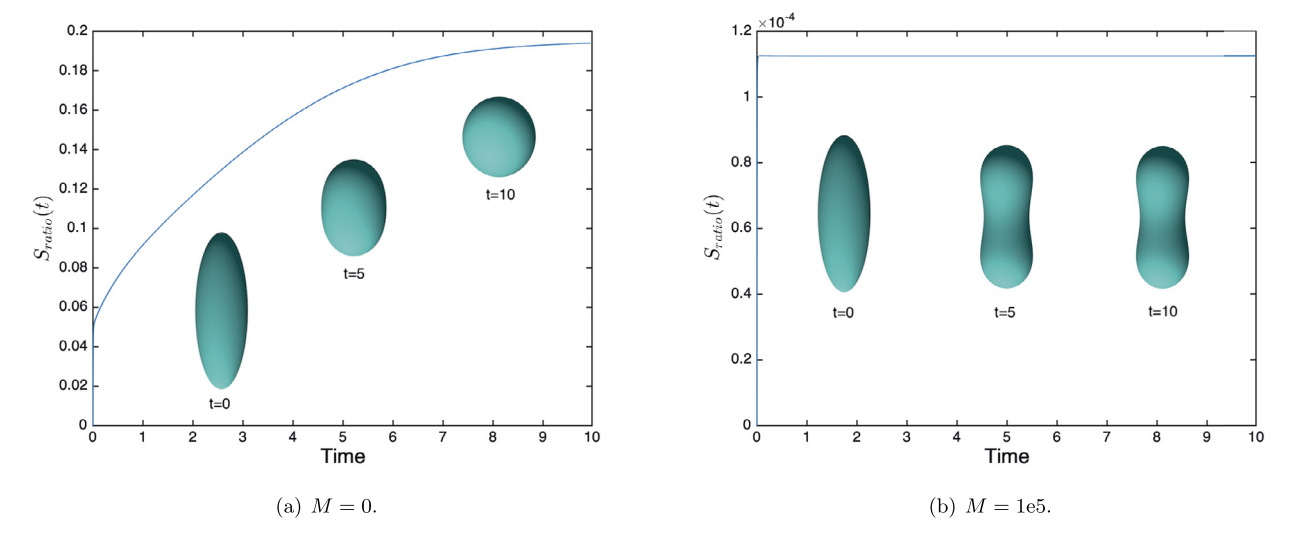


Fig. 4.10. Deformations of a narrow ellipsoid vesicle (Example 4.2.4) using two surface area parameters where (a) M=0 and (b) M=1e5. In each subfigure, we plot $S_{ratio}(t)$ with time, which is superimposed by the isosurface of $\{\phi=0\}$ at different times.

We run the simulation using two surface area parameters M=0 (non-conserved surface area) and M=1e5 (approximately conserved surface area) until the steady-state solutions are obtained. In Fig. 4.4, we plot $S_{ratio}(t)$ that changes with time, and attach the interface contour of $\{\phi=0\}$ at different times therein. It can be seen that when M=0, $S_{ratio}(t)$ eventually increases to 30%, and the shape of vesicle changes from the initial ellipse to an approximate circle. When M=1e5, $S_{ratio}(t)$ remains near 3e-3, and the final shape of the vesicle becomes a capsule shape with a thinner center and thicker ends. In Fig. 4.5, we plot the steady-state velocity field. In Fig. 4.6, we plot the time evolution of the total free energy (3.60), and attach the color graph of the steady-state pressure p as well. It can be seen that the energy decreases with time monotonically, and the contour of the pressure profile is consistent with the interface of the vesicle.

4.2.2. Deformation of two stacked circular vesicles in 2D

In this example, we study the dynamical deformation of two stacked vesicles. We set the computational domain as $\Omega = [0, 2\pi]^2$ and use the initial conditions given in (4.2). We use 257 Fourier modes to discretize the x direction, and use the Legendre polynomials up to the degree of 256 to discretize the y direction. The following parameters are used:

$$\epsilon = 0.04, \nu = 1, \gamma = 0.1, B = 1, S_1 = 4, S_2 = 4, S_3 = 1, \lambda = 0.01, \delta t = 1e - 3.$$
 (4.5)

In Fig. 4.7 (a), we plot the interface contours at different times under three different situations, where M = 0, M = 1e5, and M = 1e5 with imposed shear. For the third case, we set the boundary condition of the two components of $\mathbf{u} = (u, v)$ as

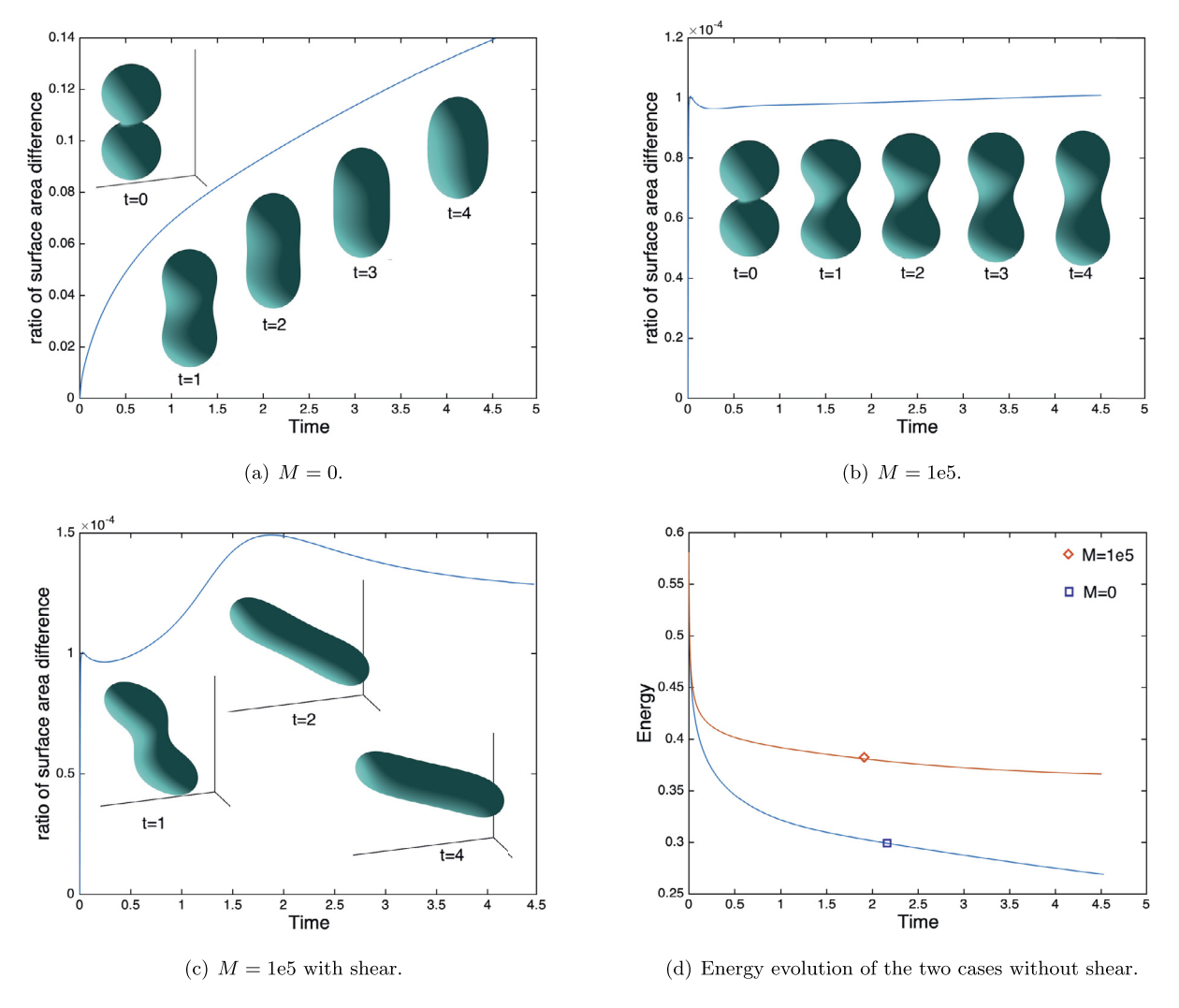


Fig. 4.11. Deformations of two 3D stacked spherical vesicles in the Example 4.2.5. In subfigures (a)-(c), we plot the time evolution of $S_{ratio}(t)$ and superimpose the isosurfaces of $\{\phi=0\}$ at various times where (a) M=0, (b) M=1e5, and (c) M=1e5. In subfigure (d), we plot the energy evolution of the two cases without shear.

 $u|_{y=2\pi}=-10$, $u|_{y=0}=10$, $v|_{y=0,2\pi}=0$. It can be seen that when M=0, the two vesicles merge and eventually converge into a wide ellipse. When M=1e5, the two vesicles eventually become a capsule shape with a thinner center and thicker ends. When M=1e5 and a shear flow is applied, the vesicles merge and then tilt along the flow direction, while maintaining the shape of the capsule. In Fig. 4.7 (b), we plot the color map of pressure p at the steady state. In Fig. 4.7 (c), we plot $S_{ratio}(t)$ that changes with time. It can be seen that for these three simulations, $S_{ratio}(t)$ finally becomes around 20% (for M=0), 3e-4 (for M=1e5 without shear), and 6e-4 (for M=1e5 with shear).

4.2.3. Deformation of five stacked circular vesicles in 2D

In this example, we set the initial conditions to five stacked circular vesicles of different sizes to study the deformation and final shape of these vesicles. The computational domain is set as $[0, 2\pi]^2$ and the initial conditions are set as follows:

$$\phi^{0} = \sum_{i=1}^{5} \tanh\left(\frac{r_{i} - \sqrt{(x - x_{i})^{2} + (y - y_{i})^{2}}}{\sqrt{2}\epsilon}\right) + 4, \mathbf{u}^{0} = \mathbf{0}, p^{0} = 0,$$
(4.6)

where $(r_1, r_2, r_3, r_4, r_5) = (0.3\pi, 0.2\pi, 0.2\pi, 0.2\pi, 0.2\pi, 0.2\pi)$, $(x_1, x_2, x_3, x_4, x_5) = (\pi, 1.5\pi, 0.5\pi, \pi, \pi)$, $(y_1, y_2, y_3, y_4, y_5) = (\pi, \pi, \pi, 1.5\pi, 0.5\pi)$. We use the following parameters

$$\epsilon = 0.08, \nu = 1, \gamma = 0.1, B = 1, S_1 = 4, S_2 = 4, S_3 = 1,$$

 $\lambda = 0.01, \delta t = 0.01/2^2, M = 1e5.$ (4.7)

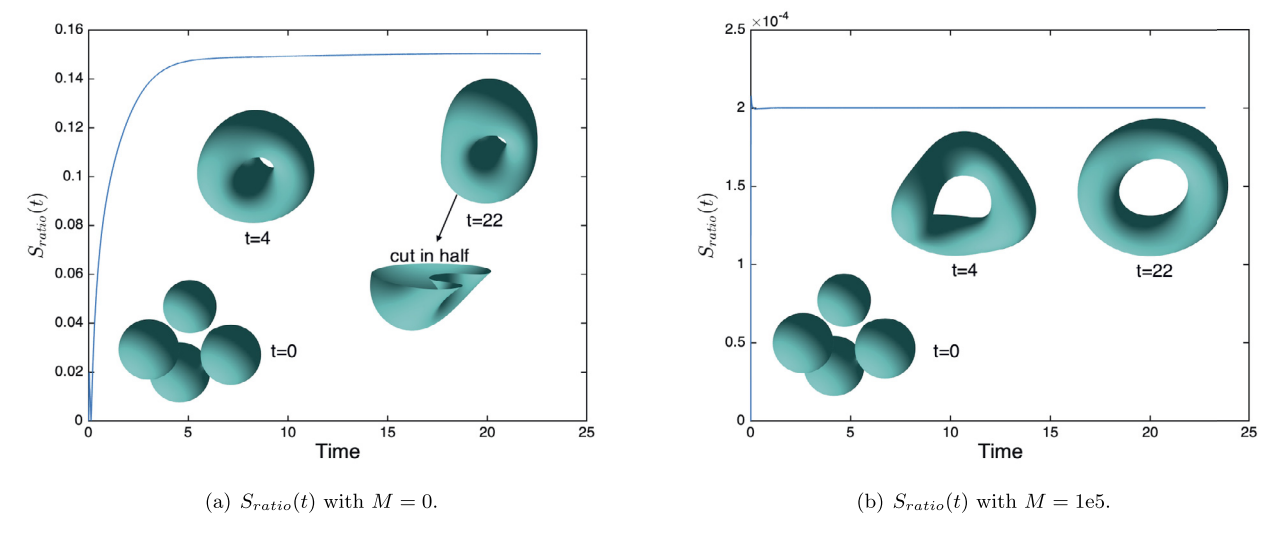


Fig. 4.12. Deformations of four 3D stacked spherical vesicles in the Example 4.2.5, where two surface area parameters are used with M = 0 and M = 1e5. In each subfigure, we plot the time evolution of $S_{ratio}(t)$ which are superimposed by the isosurfaces of $\{\phi = 0\}$ at various times.

We adopt 257 Fourier modes to discretize the x direction, and the Legendre polynomials up to the degree of 256 to discretize the y direction.

In Fig. 4.8 (a), we plot the time evolution curves of the original energy (2.1) and the modified energy (3.60). These two curves have always coincided. We impose the profiles of ϕ at three moments in Fig. 4.8 (a). It can be seen that the vesicles fuse to form a cross shape. In Fig. 4.8 (b), we plot $S_{ratio}(t)$ computed using different time steps δt . In Fig. 4.8 (c) and (d), we plot the velocity field and pressure at the steady state.

To show the effects of the stabilizers (S_i , i = 1, 2, 3), and the developed decoupling technology on improving energy stability, we perform some stability tests in which the stabilizers in (3.20) are removed and Q^{n+1} is assumed to be equal to 1 (i.e., the advection and stress are all dealt with explicitly). For convenience, we use SAV to denote this version. In Fig. 4.8 (e), we plot the energy evolutions curves computed by DSAV and SAV using different time steps. We find that all obtained energy curves computed by DSAV show monotonic attenuation. However, only when the time step is very small, the energy curve calculated by SAV decay. This illustrates the effect of stabilizers and decoupling techniques on improving stability.

4.2.4. Deformation of wide/narrow ellipsoid in 3D

In this example, we study the deformation of 3D vesicles, where the initial shape is wide ellipsoid or narrow ellipsoid respectively. The computational domain is $[0, 2\pi]^3$ and the initial conditions are set as follows:

$$\phi^{0} = \tanh\left(\frac{1 - \sqrt{(x - \pi)^{2}/r_{1} + (y - \pi)^{2}/r_{2} + (z - \pi)^{2}/r_{3}}}{\sqrt{2}\epsilon}\right), \mathbf{u}^{0} = \mathbf{0}, p^{0} = 0,$$
(4.8)

where $r_1 = r_2 = 5$, $r_3 = 1$ is the wide ellipsoid, and $r_1 = r_2 = 0.45$, $r_3 = 4$ is the narrow ellipsoid. We use the following parameters

$$\epsilon = 0.13, \nu = 1, \gamma = 0.1, B = 1, S_1 = 4, S_2 = 4, S_3 = 1, \lambda = 0.01, \delta t = 1e - 3.$$
 (4.9)

We use 129 Fourier modes to discretize each of the x and y directions, and use the Legendre polynomials up to the degree of 128 to discretize the z direction.

For the wide ellipsoid vesicle, in Fig. 4.9, we plot the time evolution of $S_{ratio}(t)$ under two surface area parameters M, and attach the snapshots of isosurface of $\{\phi=0\}$ at different times to each subfigure. When M=0, although the volume remains unchanged accurately, the ellipsoid gradually shrinks and $S_{ratio}(t)$ eventually becomes around 14%. When M=1e5, the final shape of the ellipsoid vesicle becomes the pancake shape, but the middle region is slightly thinner, and $S_{ratio}(t) \sim 3e-5$. For the narrow ellipsoid vesicle shown in Fig. 4.10, we observe that when M=0, the vesicle contracts and $S_{ratio}(t)$ eventually becomes around 20%; when M=1e5, the vesicle changes into the capsule shape with a thinner center and thicker ends, and $S_{ratio}(t)$ is around 1e-4.

4.2.5. Deformation of multiple stacked spherical vesicles in 3D

In this example, we study the dynamic deformation of multiple stacked vesicles under the action of different surface area parameter M or the shear flow applied on the domain boundary, as shown in Figs. 4.11-Fig. 4.14, respectively. We set the computational domain to $[0, L]^3$ where $L = 1.5\pi$, and the initial conditions are given as follows:

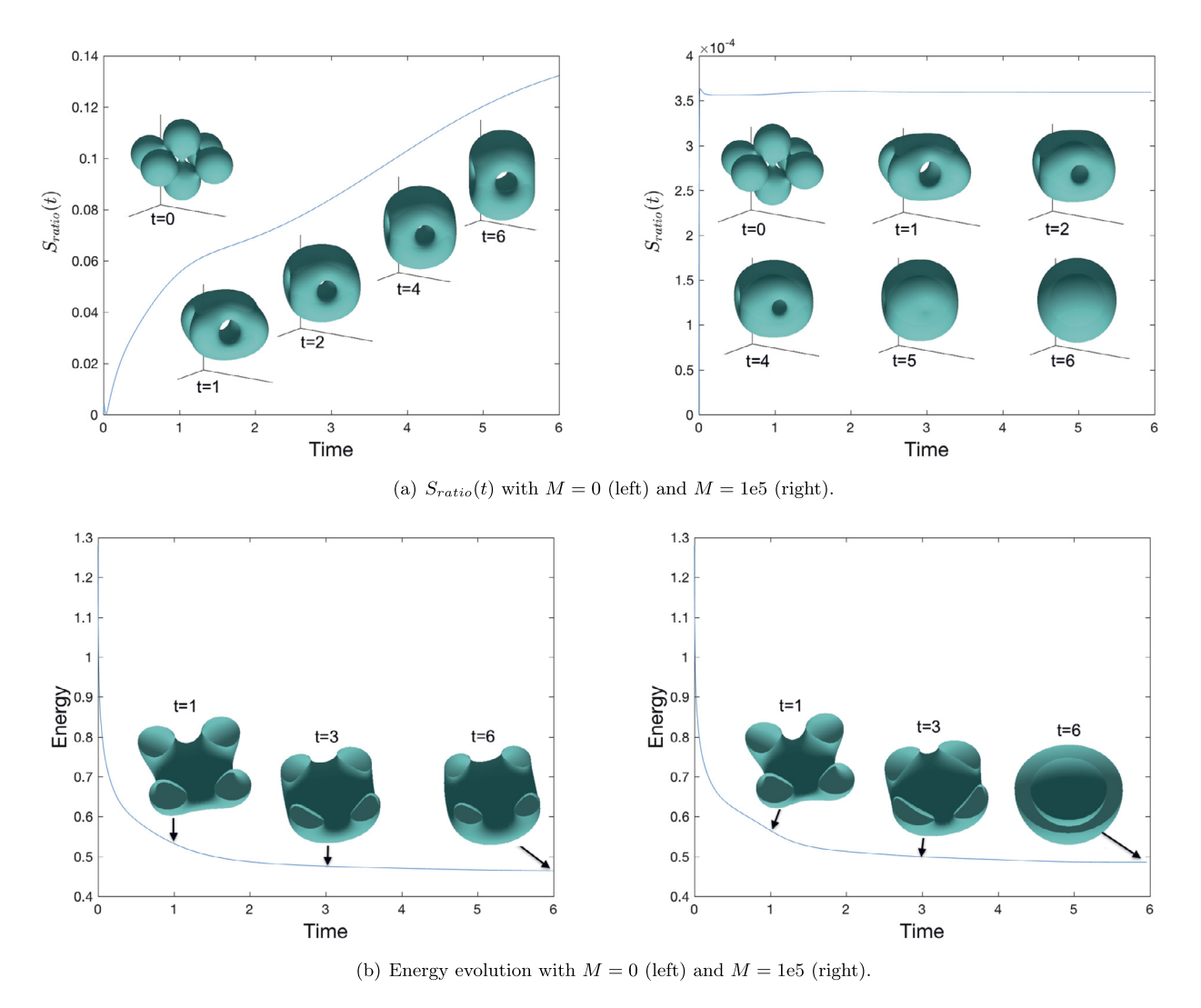


Fig. 4.13. Deformations of six 3D stacked spherical vesicles in the Example 4.2.5, where two surface area parameters are used with M=0 and M=1e5. In the subfigure (a), we plot the time evolution of $S_{ratio}(t)$ which are superimposed by the isosurfaces of $\{\phi=0\}$ at various times. In the subfigure (b), we plot the time evolution of the total free energy (2.1) which are superimposed by the isosurfaces of $\{\phi=0\}$ of half of the vesicles.

$$\phi^{0} = \sum_{i=1}^{n} \tanh\left(\frac{r_{ni} - \sqrt{(x - x_{ni})^{2} + (y - y_{ni})^{2} + (z - z_{ni})^{2}}}{\sqrt{2}\epsilon}\right) + n - 1, \mathbf{u}^{0} = \mathbf{0}, p^{0} = 0,$$

$$(4.10)$$

where n is the number of vesicles. For n=2, we set $r_{21}=r_{22}=0.14L$. $x_{21}=x_{22}=y_{21}=y_{22}=L$, $z_{21}=0.642L$, $z_{22}=0.358L$. For n=4, we set $r_{41}=r_{42}=r_{43}=0.14L$, $r_{44}=0.125L$, $x_{41}=0.3L$, $x_{42}=0.67L$, $x_{43}=0.48L$, $x_{44}=0.48L$, $y_{41}=y_{42}=y_{43}=0.5L$, $y_{44}=0.715L$, $z_{41}=z_{42}=z_{43}=0.5L$, $z_{44}=0.27L$. For n=6, we set $r_{6j,j=1,\dots,6}=0.14L$, $x_{61}=x_{62}=x_{65}=x_{66}=0.5L$, $x_{63}=0.76L$, $x_{64}=0.24L$, $y_{6j,j=1,\dots,4}=0.5L$, $y_{65}=0.76L$, $y_{66}=0.24L$, $z_{61}=0.65L$, $z_{62}=0.35L$, $z_{6j,j=3,\dots,6}=0.5L$. For n=7, we set $r_{71}=0.18L$, $r_{7j,j=2,\dots,7}=0.12L$, $x_{7j,j=1,2,3}=0.5L$, $x_{74}=0.2L$, $x_{75}=0.8L$, $x_{76}=0.2L$, $x_{77}=0.8L$, $y_{7j,j=1,\dots,5}=0.5L$, $y_{76}=0.2L$, $y_{77}=0.8L$, $z_{71}=0.5L$, $z_{72}=0.2L$, $z_{73}=0.8L$, $z_{7j,j=4,\dots,7}=0.5L$. The model parameters are set as follows:

$$\epsilon = 0.08, \nu = 1, \gamma = 0.1, B = 1, S_1 = 4, S_2 = 4, S_3 = 1, \lambda = 0.01, \delta t = 1e - 3.$$
 (4.11)

We use 129 Fourier modes to discretize each of the x and y directions, and use the Legendre polynomials up to the degree of 128 to discretize the z direction.

For n=2 (two stacked vesicles), as shown in Fig. 4.11, we can see that when M=0, the vesicles fuse and shrink, and $S_{ratio}(t)$ changes up to 14%; when M=1e5, the steady-state shape appears as a capsule and $S_{ratio}(t)$ is roughly around 1e-4. In Fig. 4.11 (c), the shear flow is imposed on the boundary ($u|_{y=L}=-10, u|_{y=0}=10$), and we can see that the vesicle is tilted in the same direction as the flow field. We plot the time evolution of the total energy for the two cases without the shear flow, as shown in Fig. 4.11 (d). For n=4 (four stacked vesicles), as shown in Fig. 4.12, we can see that

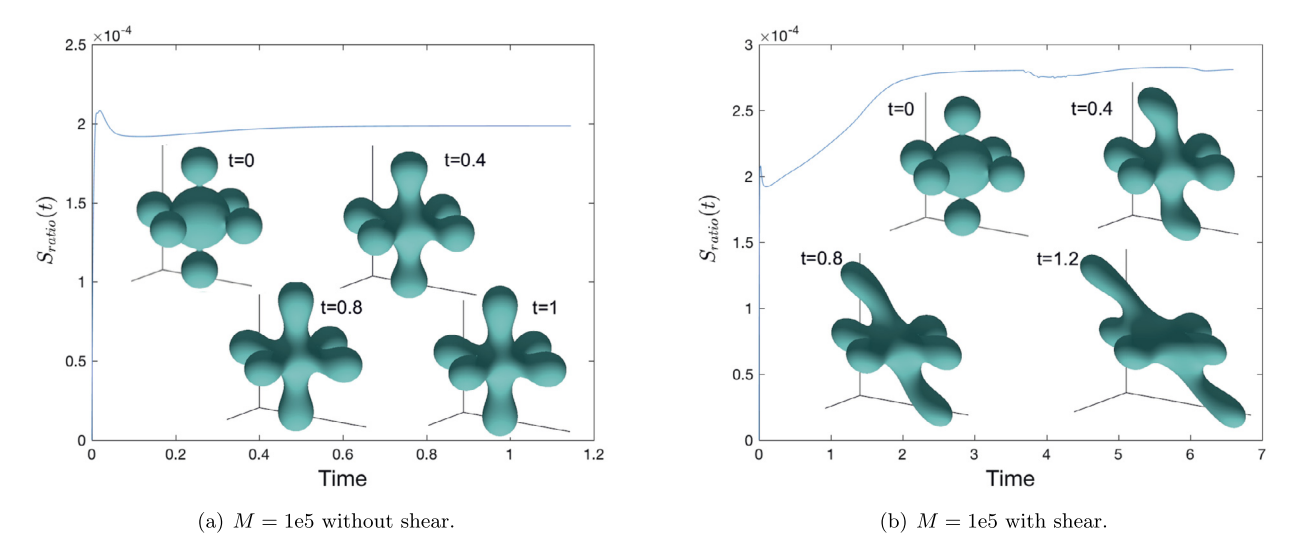


Fig. 4.14. Deformations of seven 3D stacked spherical vesicles in the Example 4.2.5, where M = 1e5 where (a) is the case without shear and (b) is with shear. In each subfigure, we plot the time evolution of $S_{ratio}(t)$ which are superimposed by the isosurfaces of $\{\phi = 0\}$ at various times.

when M=0, the vesicles fuse and shrink to form a structure with multiple poles, and $S_{ratio}(t)$ changes up to 14%; when M=1e5, the steady-state shape forms a ring and $S_{ratio}(t)$ is roughly around 2e-4. For n=6 (six stacked vesicles), we plot the time evolutions of $S_{ratio}(t)$ and the total free energy (2.1) in Fig. 4.13. To see the internal structure of the vesicle more clearly, we plot the isosurfaces of the half vesicle at various times in Fig. 4.13 (b). For n=7 (seven stacked vesicles), in Fig. 4.14, we plot $S_{ratio}(t)$ over time and the isosurface $\{\phi=0\}$ at different times. We apply shear flow at the boundary $(u|_{v=L}=-10,u|_{v=0}=10)$, which greatly affects the topological change of the vesicles, as shown in Fig. 4.14 (b).

4.3. Dynamics of a rising vesicle driven by the gravity force

In this example, we simulate the rising process of a vesicle under the action of gravity. We use the following formula to replace the momentum equation (2.5):

$$\mathbf{u}_t + (\mathbf{u} \cdot \nabla)\mathbf{u} - \nu \Delta u + \nabla p - \mu \nabla \phi = \mathbf{g}_f \phi, \tag{4.12}$$

where $\mathbf{g}_f = (0, g_f)$ for 2D, $\mathbf{g}_f = (0, 0, g_f)$ for 3D, and g_f is the pre-assumed gravity force constant. The new momentum equation (4.12) is the so-called Boussinesq approximation, where the density difference between the vesicle and the ambient fluid is assumed to be small, see [21,26,30,37].

We still perform 2D simulations first, and then perform 3D simulations. The 2D computational domain is set to be $(x, y) \in \Omega = [0, 2\pi] \times [0, 4\pi]$. We set periodic boundary conditions along the *x*-direction and discretize it using 257 Fourier modes. For the *y*-direction, we use the boundary conditions given in (3.26) and use the Legendre-Galerkin method of Legendre polynomials to the degree of 512 to discretize it. The initial conditions are set as follows,

$$\phi^{0}(x,y) = \tanh(\frac{0.4\pi - \sqrt{(x-\pi)^{2} + (y-\pi)^{2}}}{\sqrt{2}\epsilon}), \mathbf{u}^{0} = (0,0), p^{0} = 0.$$
(4.13)

The other model parameters are set as

$$\epsilon = 0.08, \nu = 1, \gamma = 0.1, B = 1, S_1 = 4, S_2 = 4, S_3 = 1, \lambda = 0.01, \delta t = 1e - 3.$$
 (4.14)

In Fig. 4.15 (a)-(c), we plot the interface contour $\{\phi=0\}$ every 0.4 time units with different surface area parameters and gravity force constants to view the complete rising process of a vesicle. It can be seen that when M=0 and $g_f=10$, shown in Fig. 4.15 (a), the vesicle eventually shows a curved shape. When we apply M=1e5 and $g_f=10$, shown in Fig. 4.15 (b), the vesicles are only slightly deforms and rises to the top in an oval shape. In Fig. 4.15 (c), we set M=1e5 and $g_f=50$. We find that the vesicle rises significantly faster, and its deformation is still very slight. In Fig. 4.15 (d), we plot the velocity field with the interface contour before the vesicle contacts the top wall. In Fig. 4.16, the change of $S_{ratio}(t)$ with time is plotted as well where S_{ratio} increases to 90% for M=0 and keeps roughly around O(1e-4) for M=1e5.

We continue to simulate the dynamical rising process of a 3D vesicle under the action of gravity. We set the calculation domain to $(x, y, z) \in \Omega = [0, 2\pi] \times [0, 2\pi] \times [0, 4\pi]$ and the initial conditions as

$$\phi^{0}(x, y, z) = \tanh(\frac{0.5\pi - \sqrt{(x-\pi)^{2} + (y-\pi)^{2} + (y-\pi)^{2}}}{\sqrt{2}\epsilon}), \mathbf{u}^{0} = (0, 0, 0), p^{0} = 0,$$

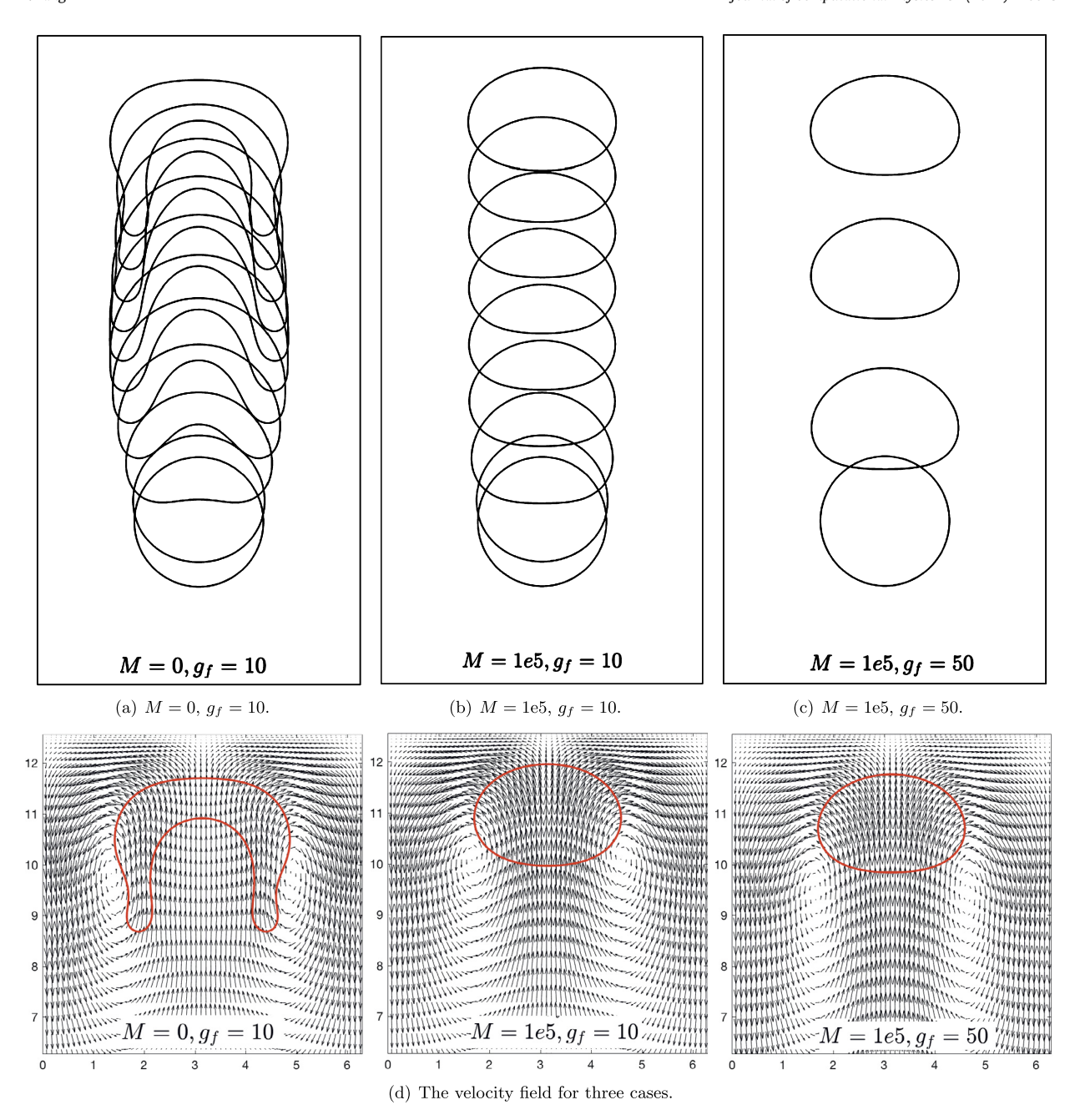


Fig. 4.15. The dynamical motions of a rising vesicle under the action of gravity where the interface contour is plotted every 0.4 time units, where (a) M = 0, $g_f = 10$, (b) M = 1e5, $g_f = 10$, (c) M = 1e5, $g_f = 50$, and (d) the velocity field with the interface contour before the vesicle touches the top wall.

All other model parameters are the same as the 2D case. Along the x and y directions, we set periodic boundary conditions and use the 257 Fourier modes to discretize each direction. For the z direction, we use the boundary conditions given in (3.26) which is discretized by using the Legendre-Galerkin method with the Legendre polynomials up to the degree of 256. In Fig. 4.17, we plot the isosurfaces of $\{\phi = 0\}$ at different times. The 3D rising dynamics is similar to the 2D simulation. When M = 0, $g_f = 50$, the vesicle finally becomes an extremely bending shape, shown in Fig. 4.17 (b), but when M = 1e5, $g_f = 50$, it can be seen that the bending of the vesicle is very small, shown in Fig. 4.17 (c).

5. Concluding remarks

We first establish a volume-conserved flow-coupled elastic bending energy model for lipid vesicles and construct a novel numerical scheme for solving it. This scheme has almost all desired properties, including linearity, second-order accuracy

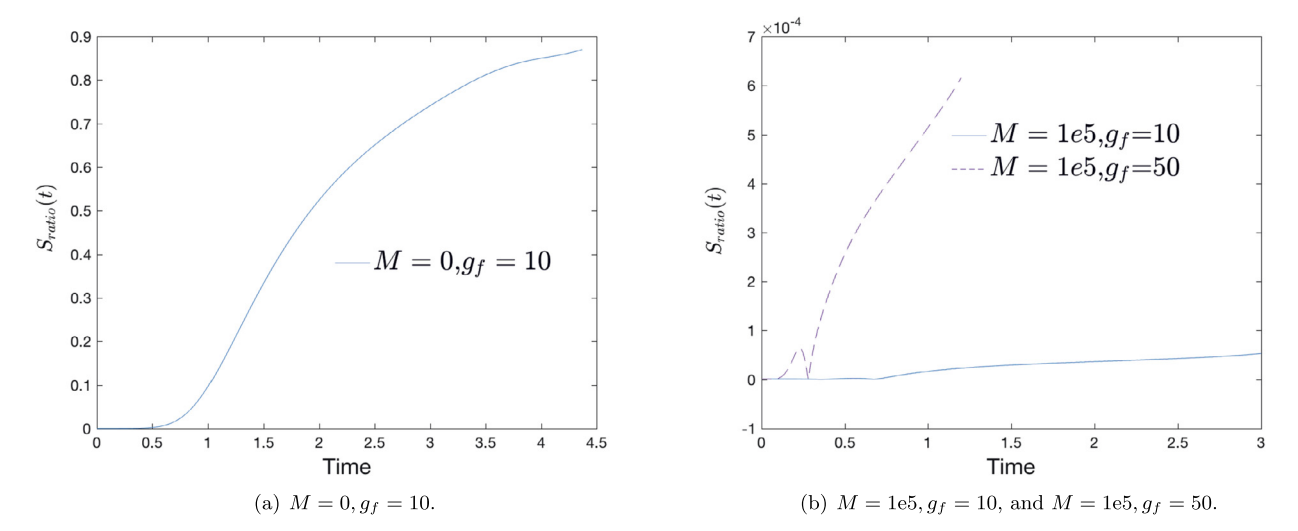


Fig. 4.16. Time evolution of $S_{ratio}(t)$ for a rising vesicle in 2D, where (a) M = 0, $g_f = 10$, (b) M = 1e5, $g_f = 10$ and $g_f = 50$.

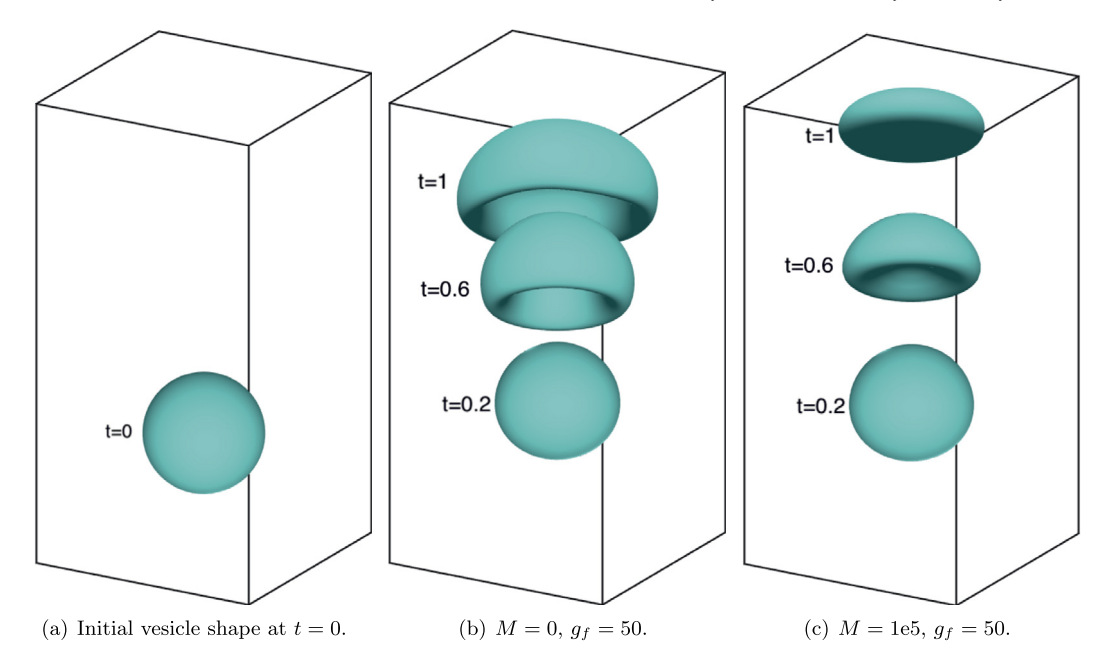


Fig. 4.17. 3D simulations of a rising vesicle with different surface area parameters, where (a) initial shape of the vesicle at t = 0, and snapshots of the vesicles at different times with (b) M = 0 and (c) M = 1e5.

in time, fully-decoupling, and unconditionally energy stability. It is based on the combination of the projection method of the Navier-Stokes equation, the SAV method of the nonlinear potential, and a new decoupling technique that deals with the coupling term with the "zero-energy-contribution" feature. We provide detailed practical methods and the rigorous proof of the unconditional energy stability and solvability. Through the simulation of many numerical examples in 2D and 3D (including convergence/stability tests, deformation of multiple stacked vesicles under the shear flow or the gravity force), the effectiveness of the model and the developed scheme are demonstrated numerically.

CRediT authorship contribution statement

This is single author paper so I take charge of everything.

Declaration of competing interest

The authors declare that they have no known competing financial interests or personal relationships that could have appeared to influence the work reported in this paper.

References

- [1] S. Aland, S. Egerer, J. Lowengrub, A. Voigt, Diffuse interface models of locally inextensible vesicles in a viscous fluid, J. Comput. Phys. 277 (2014) 32–47.
- [2] E. Bansch, A finite element pressure correction scheme for the Navier-Stokes equations with traction boundary condition, Comput. Methods Appl. Mech. Eng. 279 (2014) 198–211.
- [3] Y. Cai, H. Choi, J. Shen, Error estimates for time discretizations of Cahn-Hilliard and Allen-Cahn phase-field models for two-phase incompressible flows, Numer. Math. 137 (2017) 417–449.
- [4] C. Chen, X. Yang, Fast, provably unconditionally energy stable, and second-order accurate algorithms for the anisotropic Cahn-Hilliard model, Comput. Methods Appl. Mech. Eng. 351 (2019) 35–59.
- [5] Q. Chen, J. Shen, Multiple scalar auxiliary variable (MSAV) approach and its application to the phase-field vesicle membrane model, SIAM J. Sci. Comput. 40 (2018) A3982–A4006.
- [6] R. Chen, G. Ji, X. Yang, H. Zhang, Decoupled energy stable schemes for phase-field vesicle membrane model, J. Comput. Phys. 302 (2015) 509–523.
- [7] A. Diegel, C. Wang, X. Wang, S. Wise, Convergence analysis and error estimates for a second order accurate finite element method for the Cahn-Hilliard-Navier-Stokes system, Numer. Math. 137 (2017) 495–534.
- [8] Q. Du, M. Li, C. Liu, Analysis of a phase field Navier-Stokes vesicle-fluid interaction model, Discrete Contin. Dyn. Syst., Ser. B 8 (3) (2007) 539-556.
- [9] Q. Du, C. Liu, X. Wang, A phase field approach in the numerical study of the elastic bending energy for vesicle membranes, J. Comput. Phys. 198 (2004) 450–468.
- [10] Q. Du, C. Liu, X. Wang, Simulating the deformation of vesicle membranes under elastic bending energy in three dimensions, J. Comput. Phys. 212 (2005) 757–777.
- [11] X. Feng, Fully discrete finite element approximations of the Navier-Stokes-Cahn-Hilliard diffuse interface model for two-phase fluid flows, Modél. Math. Anal. Numér. 44 (2006) 1049–1072.
- [12] C. Funkhouser, F. Solis, K. Thorton, Coupled composition-deformation phase-field method for multicomponent lipid membranes, Phys. Rev. E 76 (2007) 011912.
- [13] J.L. Guermond, P. Minev, J. Shen, An overview of projection methods for incompressible flows, Comput. Methods Appl. Mech. Eng. 195 (2006) 6011–6045.
- [14] J.L. Guermond, L. Quartapelle, A projection FEM for variable density incompressible flows, J. Comput. Phys. 165 (1) (2000) 167-188.
- [15] J.L. Guermond, A. Salgado, A splitting method for incompressible flows with variable density based on a pressure Poisson equation, J. Comput. Phys. 228 (2009) 2834–2846.
- [16] J.-L. Guermond, Abner J. Salgado, Error analysis of a fractional time-stepping technique for incompressible flows with variable density, SIAM J. Numer. Anal. 49 (3) (2011) 917–944.
- [17] F. Guillen-Gonzalez, G. Tierra, Unconditionally energy stable numerical schemes for phase-field vesicle membrane model, J. Comput. Phys. 354 (2018) 67–85.
- [18] D. Han, X. Wang, A second order in time, uniquely solvable, unconditionally stable numerical scheme for Cahn-Hilliard-Navier-Stokes equation, J. Comput. Phys. 290 (2015) 139–156.
- [19] D. Kay, V. Styles, R. Welford, Finite element approximation of a Cahn-Hilliard-Navier-Stokes system, Interfaces Free Bound. 10 (2008) 15-43.
- [20] S. Lee, A. Salgado, Stability analysis of pres- sure correction schemes for the Navier-Stokes equations with traction boundary conditions, Comput. Methods Appl. Mech. Eng. 309 (2016) 307–324.
- [21] C. Liu, J. Shen, A phase field model for the mixture of two incompressible fluids and its approximation by a Fourier-spectral method, Physica D 179 (3-4) (2003) 211-228.
- [22] J. Lowengrub, A. Ratz, A. Voigt, Phase-field modeling of the dynamics of multicomponent vesicles: spinodal decomposition, coarsening, budding, and fission, Phys. Rev. E 79 (2009) 031926.
- [23] S. Minjeaud, An unconditionally stable uncoupled scheme for a triphasic Cahn–Hilliard/Navier–Stokes model, Numer. Methods Partial Differ. Equ. 29 (2) (2013) 584–618.
- [24] R. Nochetto, J.-H. Pyo, The gauge-Uzawa finite element method part I: the Navier-Stokes equations, SIAM J. Numer. Anal. 43 (2005) 1043-1068.
- [25] J. Pyo, J. Shen, Gauge-Uzawa methods for incompressible flows with variable density, J. Comput. Phys. 221 (2007) 181-197.
- [26] T. Qin, S. Ragab, P. Yue, Axisymmetric simulation of the interaction of a rising bubble with a rigid surface in viscous flow, Int. J. Multiph. Flow 52 (2013) 60–70.
- [27] J. Rubinstein, P. Sternberg, Nonlocal reaction-diffusion equations and nucleation, IMA J. Appl. Math. 48 (1992) 249-264.
- [28] J. Shen, J. Xu, J. Yang, The scalar auxiliary variable (SAV) approach for gradient flows, J. Comput. Phys. 353 (2018) 407-416.
- [29] J. Shen, X. Yang, A phase-field model and its numerical approximation for two-phase incompressible flows with different densities and viscosities, SIAM J. Sci. Comput. 32 (2010) 1159–1179.
- [30] J. Shen, X. Yang, Decoupled energy stable schemes for phase filed models of two phase complex fluids, SIAM J. Sci. Comput. 36 (2014) B122-B145.
- [31] J. Shen, X. Yang, Decoupled, energy stable schemes for phase-field models of two-phase incompressible flows, SIAM J. Numer. Anal. 53 (1) (2015) 279–296.
- [32] J. Shen, X. Yang, H. Yu, Efficient energy stable numerical schemes for a phase field moving contact line model, J. Comput. Phys. 284 (2015) 617-630.
- [33] D. Siegel, M. Kozlov, The Gaussian curvature elastic modulus of N-monomethylated dioleoylphosphatidylethanolamine: Relevance to membrane fusion and lipid phase behavior, Biophys. J. 87 (2004) 366–374.
- [34] J. van Kan, A second-order accurate pressure-correction scheme for viscous incompressible flow, SIAM J. Sci. Stat. Comput. 7 (3) (1986) 870-891.
- [35] X. Wang, Q. Du, Modelling and simulations of multi-component lipid membranes and open membranes via diffusive interface approaches, J. Math. Biol. 56 (2008) 347–371.
- [36] X. Wang, L. Ju, Q. Du, Efficient and stable exponential time differencing Runge-Kutta methods for phase field elastic bending energy models, J. Comput. Phys. 316 (2016) 21–38.
- [37] X. Yang, J.J. Feng, C. Liu, J. Shen, Numerical simulations of jet pinching-off and drop formation using an energetic variational phase-field method, J. Comput. Phys. 218 (2006) 417–428.
- [38] X. Yang, L. Ju, Efficient linear schemes with unconditionally energy stability for the phase field elastic bending energy model, Comput. Methods Appl. Mech. Eng. 315 (2017) 691–712.
- [39] J. Zhang, S. Das, Q. Du, A phase field model for vesicle-substrate adhesion, J. Comput. Phys. 228 (2009) 7837-7849.
- [40] J. Zhang, X. Yang, Decoupled, non-iterative, and unconditionally energy stable large time stepping method for the three-phase Cahn-Hilliard phase-field model, J. Comput. Phys. 404 (2020) 109115.
- [41] J. Zhang, X. Yang, Unconditionally energy stable large time stepping method for the L2-gradient flow based ternary phase-field model with precise nonlocal volume conservation, Comput. Methods Appl. Mech. Eng. 361 (2020) 112743.